Influence of stochastic perturbations of composite laminate layups on the aeroelastic flutter of a cantilevered plate wing

Christian Nitschke[a], Angela Vincenti[a], Jean-Camille Chassaing[a,*]

[a]*Sorbonne Université, CNRS, Institut Jean Le Rond d'Alembert, UMR 7190, F-75005 Paris, France*

Abstract

A numerical study of the effect of uncertainties in ply angles and thicknesses on the flutter speed of a cantilevered composite plate wing was conducted in this paper. Reduction of the number of uncertain parameters was possible thanks to the use of the polar method, which also enabled a systematic analysis of the influence of material symmetries. From the polar domain of orthotropic laminates, several stacking sequences were reconstructed in order to propagate parametric uncertainties. Typical fabrication uncertainties on ply thicknesses and angles were were considered in order to quantify their influence on the probabilistic aeroelastic response. The reduction of the set of stochastic parameters by the polar method enabled the use of a polynomial-chaos approach which was combined with machine-learning techniques in order to deal with the correlation and with discontinuities in the response surface. Results reveal that possible manufacturing tolerances cause significant deviations in the critical flutter speed from the nominal value, especially when mode switches occur. As these deviations surpass classical dimensioning margins, uncertainty quantification approaches can provide added safety.

1. Introduction

As they have a high strength- and stiffness-to-weight ratio, composite materials are increasingly employed in structural design in aeronautics. Moreover, the anisotropy of their stiffness permits adaption of the material to aeroelastic requirements, a process which is known as aeroelastic tailoring. This allows for improvements of performance and economy in modern aircraft.

However, anisotropy introduces a certain amount of challenges in the design of composite structures. When considering the dynamical behaviour, systematic studies of composite plates in free vibration have begun at the end of the 1960s and the beginning of the 1970s [1, 2]. Interest in using composite plates for dealing with aeroelastic problems rose soon, with the first studies conducted by Ramkumar and Weisshaar [3]. Intensive theoretical and experimental research has been carried out afterwards: pioneering work on aeroelastic tailoring [4, 5, 6] was accompanied by parameter studies in free vibration and aeroelasticity [7, 8, 9, 10].

Studies of uncertainty quantification on composite plates and especially on their vibration behaviour appeared in the late 1980s, as in [11]. Recent years have seen a renaissance of interest in uncertainty quantification with respect to the vibratory behaviour, where the authors take

*Corresponding author

Email addresses: christian@nitschke.org (Christian Nitschke), angela.vincenti@sorbonne-universite.fr (Angela Vincenti), jean-camille.chassaing@sorbonne-universite.fr (Jean-Camille Chassaing)

special interest in the layup effects, and forward as well as inverse uncertainty propagation is performed [12, 13, 14, 15]. Interest has consequently been picked up in the field of aeroelasticity [16, 17]. A recent research by Scarth et al. [18] considered laminated composite materials and performed forward quantification of uncertainties in ply angles on the flutter speed of a cantilever wing, with a restriction to symmetric layup configurations.

Analysing individual ply angles and ply thicknesses, when they are combined in the laminate stacking sequence with rising number of plies, becomes quickly too complex to draw meaningful conclusions on the laminate's global behaviour. This is why, at the end of the 1970s/the beginning of the 1980s, different approaches were developed in order to provide more synthetic parameters for the analysis and design of composite laminates. Tsai and Hahn [19] introduced the concept of lamination parameters. Roughly at the same time, Verchery [20] developed the polar method, which is based on tensor invariants and is thus more general [21]. Whilst the early is more widely used, the latter has seen considerable work in the 2000s: the polar method was applied in the formulation of optimal design problems for composite structures [21, 22, 23, 24], and thermodynamic and geometric bounds [23, 24, 25] were defined for the existence of laminates in the space of polar parameters. Lamination parameters as well as polar parameters are invariants with a change in the laminate's reference frame, i.e. they represent intrinsic material properties for the anisotropic behaviour of the laminate. Particularly, polar invariants give precise informations on material symmetries. In addition, both approaches need a fixed number of twelve and eighteen parameters respectively in order to represent the general behaviour of a laminate. This set can be even further reduced depending on the behaviour of interest. In the case of the deterministic optimisation of orthotropic laminated structures, the problem can be limited to a minimal set of two polar parameters, as shown in [23, 24, 26, 27]. This is a significant advantage with respect to the direct use of the laminate's constitutive parameters (ply angles and thicknesses), since their number is directly proportional to the number of plies in the stack and it can rapidly raise to several tenths when dealing with laminates for structural applications.

Either the lamination parameters approach or the polar method reduce the number of representative parameters of the laminate, which is an advantage when dealing with optimisation problems or stochastic studies of composite structures [18]. However, whilst ply constitutive parameters can be considered as independent variables, lamination or polar parameters are correlated because they are constructed on common aggregates of the same sets of ply properties linking the variations. This fact can be a difficulty in the stochastic analysis of composite structures.

The polynomial-chaos techniques often used in structural problems originate in [28], where they were written for independent Gaussian distributions. Xiu and Karniadakis [29] generalised them to a whole set of different distributions contained in the so-called Askey-scheme, and was quickly applied to fluid dynamics [30, 31] and fluid-structure interaction problems [32, 33]. However, these techniques can only deal with a limited number of independent stochastic variables with well-known distributions. While advanced techniques based on sensitivity analysis permit direct application of polynomial chaos techniques on ply angles and ply thicknesses (e. g. [34]), these methods are still overwhelmed by the number of parameters when confronted with typical numbers of plies in aeronautic applications. Lamination or polar parameters reduce the number of parameters, but have the inconvenience that their distributions are correlated and difficult to characterise, having no equivalent in the Askey scheme used for standard generalised polynomial chaos.

Thus, some modifications of the classical techniques are introduced. In order to treat the correlation, authors used decomposition procedures such as Karhunen-Loève decompositions [35] or Rosenblatt transformation [18]. However, these methods either make strong assumptions about the correlations as in the first case, or require the inverse of conditional CDFs as in the latter, which are tedious to compute or approximate. Soize and Ghanem [36] described

a framework for applying polynomial chaos to arbitrary distributions. Navarro et al. [37] demonstrated its use on correlated distributions. An approach of this family has already been used by Dey et al. [38] in the context of an uncertainty study on a laminated plate in free vibration, where it was used on individual, non-correlated variables in a fuzzy analysis. A stochastic finite element study of fiber-reinforced laminate based on an approximation of the random field using truncated Karhunen-Loève expansion was conducted in [39].

In this work, we will study the effect of typical fabrication errors in composite layups on the aeroelastic behaviour of a rectangular cantilevered composite plate wing. In addition to ply angles already treated by Scarth et al. [18], ply thicknesses will be incorporated in the study and the hypothesis of symmetric and uncoupled stacking sequence will be realeased, so as to study more general stacks and take into account the effect of non-zero membrane-bending coupling. The study of the uncertainty in critical flutter velocity shows the advantages of probabilistic evaluation over classical flutter qualification. In section 2, the aeroelastic example model will be presented along with the instability solving method which will be used to determine the critical flutter velocity, the mode shapes and the corresponding frequency. Section 3 gives a summary of the polar method, which reduces the number of parameters and helps thus with the interpretation of the material stiffness properties of the composite laminate layups. It will serve as the principal tool of analysis and enables the use of response surface technologies. In Section 4, the deterministic aeroelastic response in the polar domain will be examined. Special attention will be paid to switches in modal behaviour, which significantly alter the response in critical flutter velocity and flutter frequency. This preliminary analysis will allow to choose pertinent configurations of which the stochastic properties will be studied in Section 5.

2. Aeroelastic Problem

In this study, we analyse the aeroelastic response of a straight-wing model, composed of a flat cantilevered laminated composite plate. This model is largely similar to that of [40, 18]. The associated aerodynamics is represented by a strip-theory potential-flow model. Despite its numerous simplifications, this model permits to highlight the main interesting phenomena, i.e. the effect of the anisotropic behaviour of composite laminates and particularly the emergence of mode switches leading to discontinuities in the aeroelastic response. A scheme of the wing is given in Fig. 1.

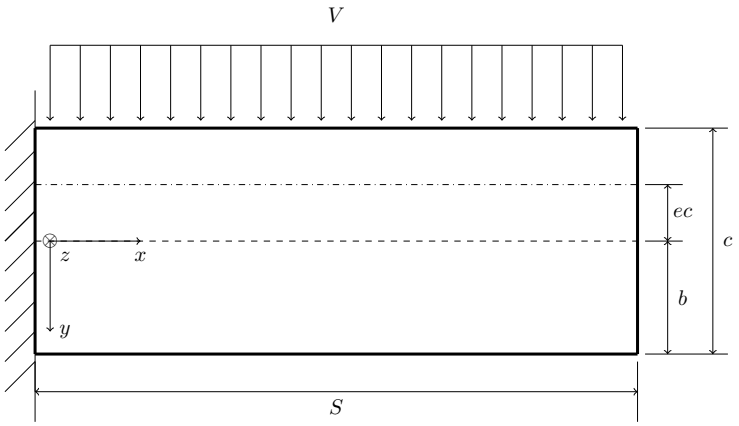

Figure 1: Scheme of the cantilevered plate wing

We note S the half span, c the chord, and b the half chord as illustrated in Fig. 1. The reference axis is the x axis, which is situated mid-chord. This is also set as the reference axis for the composite fibre direction. The axis of application of the aeroelastic line forces and moments is offset from the x axis by $-ec$, where e is called the excentricity factor, rendered dimensionless by the chord length. This excentricity factor is set to $e = \frac{1}{4}$ throughout the paper, which corresponds to the standard value for a flat plate. The freestream velocity V is assumed to be aligned with the y axis, and the z direction is pointing downwards.

In the following, we will perform aeroelastic simulations on wings as presented in Fig. 1 with the geometric and aeromechanical parameters presented in Table 1

Wing half span $S[m]$	Chord $c[m]$	Air density ρ_a $\left[kg/m^3\right]$	Lift excentricity e	Unsteady parameter $M_{\dot{\theta}}$
0.3048	0.0762	1.225	0.25	-1.2

Table 1: Wing geometry and aeromechanical data ([40, 18])

The elastic behaviour of the wing is modelled following classical laminated plate theory. The relation between generalised forces and displacements are given in that framework as [41]

$$\begin{bmatrix} \mathbf{n} \\ \mathbf{m} \end{bmatrix} = \begin{bmatrix} \mathbf{A} & \mathbf{B} \\ \mathbf{B} & \mathbf{D} \end{bmatrix} \begin{bmatrix} \boldsymbol{\varepsilon} \\ \boldsymbol{\kappa} \end{bmatrix} \tag{1}$$

where $\mathbf{n}$ and $\mathbf{m}$ are the membrane forces and bending moments, $\mathbf{A}$ is the membrane stiffness, $\mathbf{D}$ the bending stiffness and $\mathbf{B}$ describes the coupling between the membrane and the bending forces. The curvature $\boldsymbol{\kappa}$ and the in-plane strain $\boldsymbol{\varepsilon}$ of the composite plate are defined as

$$\boldsymbol{\kappa} = \begin{pmatrix} -\frac{\partial^2 w}{\partial x^2} \\ -\frac{\partial^2 w}{\partial y^2} \\ -2\frac{\partial^2 w}{\partial x \partial y} \end{pmatrix} \tag{2}$$

$$\boldsymbol{\varepsilon} = \begin{pmatrix} \frac{\partial u}{\partial x} \\ \frac{\partial v}{\partial y} \\ \frac{\partial u}{\partial y} + \frac{\partial w}{\partial x} \end{pmatrix} \tag{3}$$

Considering pure bending loads ($\mathbf{n} = 0$), Eq. 1 can be rewritten in terms of the moments $\mathbf{m}$ only as

$$\mathbf{m} = \left(\mathbf{D} - \mathbf{B}\mathbf{A}^{-1}\mathbf{B}\right)\boldsymbol{\kappa} \tag{4}$$

where we call

$$\tilde{\mathbf{D}} = \mathbf{D} - \mathbf{B}\mathbf{A}^{-1}\mathbf{B} \tag{5}$$

the modified bending stiffness matrix [42]. Tensor $\tilde{\mathbf{D}}$ thus contains the information of coupling tensor $\mathbf{B}$. Consequently, it is valid for a general laminate's stacking sequence, which is not necessarily uncoupled or symmetric. However, when there is no coupling and $\mathbf{B} = 0$, then tensor $\tilde{\mathbf{D}}$ reduces to bending stiffness tensor $\mathbf{D}$.

The equations of the dynamic behaviour of the wing subject to aerodynamic loads are written in the Lagrangian formalism. The elastic potential energy of the plate under bending load is [43]

$$U = \frac{1}{2}\int\int \mathbf{m}^{\mathsf{T}}\boldsymbol{\kappa} dxdy \tag{6}$$

This expression can be expanded using Eq. (4) to

$$U = \frac{1}{2}\int\int \boldsymbol{\kappa}^{\mathsf{T}}\tilde{\mathbf{D}}\boldsymbol{\kappa} dxdy \tag{7}$$

The kinetic energy is given by [40]

$$T = \frac{1}{2}\rho d \int\int \dot{w}^2 dxdy \tag{8}$$

where the dot above the displacement denotes a derivative with respect to time, d is the total thickness of the plate and ρ is the density of the plate material.
Finally the virtual work of the aerodynamic lift and moment is obtained by [44]

$$\delta W = \int l_a(-\delta w)dx + \int m_a \delta\theta dx \tag{9}$$

where the expressions for the line lift l_a and the line moment m_a are given by quasi-steady strip theory as [40]

$$l_a = \frac{1}{2}\rho_a V^2 c a_w \left(\theta + \frac{\dot{w}}{V}\right) \tag{10}$$

$$m_a = \frac{1}{2}\rho_a V^2 c^2 \left(e a_w \left(\theta + \frac{\dot{w}}{V}\right) + M_{\dot{\theta}} \frac{\dot{\theta} c}{4V}\right) \tag{11}$$

being θ the rotation of wing section around the y-axis, ρ_a the air density, $a_w = 2\pi\left(1 - \left(\frac{x}{S}\right)^3\right)$ the lift-curve slope along the span, and $M_{\dot{\theta}}$ is an approximation of the unsteady aerodynamic moment derivative, which is assumed constant with $M_{\dot{\theta}} = -1.2$ as in [40].

The equilibrium problem is formulated in the Lagrangian formalism as

$$\frac{d}{dt}\left(\frac{\partial T}{\partial \dot{\mathbf{q}}}\right) - \frac{\partial T}{\partial \mathbf{q}} + \frac{\partial U}{\partial \mathbf{q}} = \frac{\partial(\delta W)}{\partial(\delta \mathbf{q})} \tag{12}$$

where $\mathbf{q}$ is the vector of Lagrangian generalised coordinates.

In order to solve the equilibrium problem (12), we apply a Rayleigh-Ritz approximation of the displacements w, as combination of simple algebraic polynomials [45]

$$w(x,y) = \sum_{i=1}^{n_x}\sum_{j=1}^{n_y} q_{(ij)}(t)\left(\frac{x}{S}\right)^{i+1}\left(\frac{y}{c}\right)^{j-1} \tag{13}$$

where n_x and n_y is the number of the monomial terms in the x- and y-coordinate respectively and the generalised Lagrangian coordinate $q_{(ij)}$ is defined as a function of time:

$$q_{(ij)}(t) = \hat{q}_{(ij)} \exp(\imath\omega t) \quad , \quad (i = 1, ..., n_x; j = 1, ..., n_y) \tag{14}$$

Finally, angle θ in Eq. (10) is derived using an assumption of small displacements as $\theta = \frac{\partial w}{\partial x}$.

Using the Lagrange formalism of Eq. (12) and substituting Eq. (13) into Eqs. (7,8,9), the equations of motion can be given as [44]

$$\mathbf{M}_{struct}\ddot{\mathbf{q}} + \mathbf{K}_{struct}\mathbf{q} = \mathbf{D}_{aero}\dot{\mathbf{q}} + \mathbf{K}_{aero}\mathbf{q} \tag{15}$$

which can be reformulated as a generalised eigenvalue problem [44] in terms of the vector $\hat{\mathbf{q}}$ of the $n_x \times n_y$ amplitude coefficients $\hat{q}_{(ij)}$

$$\begin{bmatrix} \mathbf{0} & \mathbf{I} \\ (\mathbf{K}_{aero} - \mathbf{K}_{struct}) & \mathbf{D}_{aero} \end{bmatrix} \begin{bmatrix} \hat{\mathbf{q}} \\ \lambda\hat{\mathbf{q}} \end{bmatrix} = \begin{bmatrix} \mathbf{I} & \mathbf{0} \\ \mathbf{0} & \mathbf{M}_{struct} \end{bmatrix} \lambda \begin{bmatrix} \hat{\mathbf{q}} \\ \lambda\hat{\mathbf{q}} \end{bmatrix} \tag{16}$$

where $\mathbf{M}_{struct}$ denotes the structural mass matrix, $\mathbf{D}_{aero}$ the aerodynamic damping matrix, $\mathbf{K}_{aero}$ the aerodynamic stiffness matrix and $\mathbf{K}_{struct}$ the elastic stiffness matrix. The eigenvalue is defined as $\lambda = -\zeta\omega \pm \imath\omega\sqrt{1-\zeta^2}$, so the wing enters in instability for $\mathfrak{Re}(\lambda) > 0$, *i.e.* $\zeta < 0$. For the limit of instability $\zeta = 0$, the expression for the eigenvalues simplifies to $\lambda = \imath\omega$ and $\lambda^2 = -\omega^2$.

An example of flutter diagram (namely the $V - \lambda$ diagram) with a selection of modes is given in Fig. 2, which is calculated using the geometry and aeromechanical parameters from Table 1. A 1mm-thick steel plate was considered with Young's modulus $E = 210\,[GPa]$ and Poisson coefficient $\nu = 0.3$. Fig. 2(a) shows the real part of the eigenvalues as a function of the velocity. As it can be deduced from the instability condition given above, the flutter velocity is the lowest velocity for which the real part of the eigenvalue passes though the zero, switching its sign from negative to positive. This point is indicated by the black vertical bar. The corresponding flutter mode is thus the green curve. The frequency in that point can be found using the right part of the diagram Fig. 2(b), where the flutter velocity is again indicated by the black vertical bar. The flutter frequency is found on the curve that corresponds to the flutter mode in the left part of the figure which is again indicated by green lines. It is noted that the eigenvalues occur in complex conjugate pairs. This is why there are two corresponding lines for each mode in part (b) of the figure. In this case, flutter occurs at $V_f = 68.41\,[m/s]$ and at a circular frequency of $\omega = 408.9\,[rad/s]$.

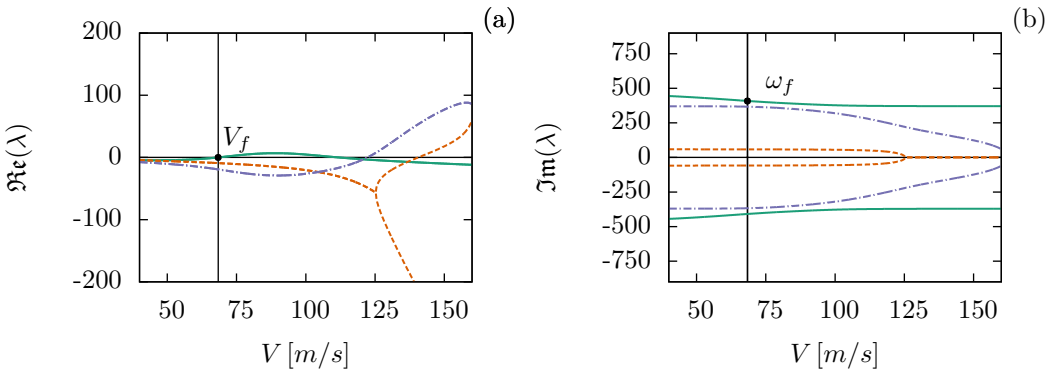

Figure 2: Example $V - \lambda$ diagram for a 1mm-thick steel plate with the geometry given in Table 1. The critical flutter velocity of $68.41\,[m/s]$ is indicated by the black vertical bar on the left. On the right, the flutter frequency of $408.9\,[rad/s]$ is given.

3. The Polar Method

Despite not being the only factor, the behaviour of the structure has a significant influence on the aeroelastic response of the system presented in the previous section. In the case of a cantilever wing made of a laminated composite plate, the plate's behaviour can be simply represented in terms of a single stiffness tensor $\tilde{\mathbf{D}}$, as shown in Eq. (5). However, this modified bending stiffness tensor is generally anisotropic, which is difficult to represent and to interpret.

The elastic behaviour of laminates is often represented using the so-called *lamination parameters* [19], which are sums of sinuses and cosinuses of angles in the laminate's stack. Lamination parameters have the advantage to be invariant for a rotation of the plate's reference frame and, for this reason, they have been widely used in the formulation of design and optimisation

problems for laminates [46, 47, 48]. However, lamination parameters are defined for laminates with identical layers (same ply material and same ply thickness throughout the sequence), so that they cannot easily account for layers of different thickness. In addition, they are expressed for the laminate's stiffness behaviour only (tensors $\mathbf{A}$, $\mathbf{D}$ or $\mathbf{B}$) and they cannot be directly applied to the representation of the modified stiffness tensor $\tilde{\mathbf{D}}$ introduced in Eq. (5).

In order to give an intrinsic representation of the plate anisotropic behaviour which holds valid in the case of different plies in the stack as well as for the modified stiffness tensor $\tilde{\mathbf{D}}$, we adopt the polar formalism [20, 21] which allows to represent any anisotropic tensor in the plane in terms of polar invariants and angles. In the case of a fourth-order stiffness tensor $\mathbf{Q}$ representing the rigidity of a general anisotropic material layer, the polar decomposition is described as follows [21]

$$
\begin{aligned}
8T_0 &= Q_{xx} - 2Q_{xy} + 4Q_{ss} + Q_{yy} && (17)\\
8T_1 &= Q_{xx} + 2Q_{xy} + Q_{yy} && (18)\\
8R_0 e^{\imath 4\Phi_0} &= Q_{xx} + 4\imath Q_{xs} - 2Q_{xy} - 4Q_{ss} - 4\imath Q_{ys} + Q_{yy} && (19)\\
8R_1 e^{\imath 2\Phi_1} &= Q_{xx} + 2\imath Q_{xs} + 2\imath Q_{ys} - Q_{yy} && (20)
\end{aligned}
$$

where $Q_{\alpha\beta}$ are the Cartesian components of tensor $\mathbf{Q}$ (indexes x and y refer to the axis coordinates, whilst s stands for *shear*). The same relations hold for the laminate's tensors $\mathbf{A}$, $\mathbf{D}$ and $\mathbf{B}$, as well as for the modified bending stiffness $\tilde{\mathbf{D}}$. In Eqs. (17)-(20), positive scalars T_0 and T_1 represent the isotropic part of the stiffness, whereas R_0 and R_1 represent the modules of the anisotropic behaviour. Φ_0 and Φ_1 denote the angles of the deviation of the anisotropic material behaviour with respect to the reference axis. Quantities T_0, T_1, R_0, R_1 and $(\Phi_0 - \Phi_1)$ are invariants, while angles Φ_0 and Φ_1 depend on the choice of the reference frame.

The inverse of the operations (17)-(20) give the cartesian representation of the stiffness tensor in terms of the polar constants [21]

$$
\begin{aligned}
Q_{xx} &= T_0 + 2T_1 + R_0\cos(4\Phi_0) + 4R_1\cos(2\Phi_1) && (21)\\
Q_{xy} &= -T_0 + 2T_1 - R_0\cos(4\Phi_0) && (22)\\
Q_{xs} &= R_0\sin(4\Phi_0) + 2R_1\sin(2\Phi_1) && (23)\\
Q_{yy} &= T_0 + 2T_1 + R_0\cos(4\Phi_0) - 4R_1\cos(2\Phi_1) && (24)\\
Q_{ys} &= -R_0\sin(4\Phi_0) + 2R_1\sin(2\Phi_1) && (25)\\
Q_{ss} &= T_0 - R_0\cos(4\Phi_0) && (26)
\end{aligned}
$$

A significant advantage of the polar method is that it allows to easily determine material symmetries [21]. In the isotropic case, the anisotropic invariants R_0 and R_1 are obviously zero. Square-symmetry is expressed when only the fourth-order harmonic of module R_0 persists (see eq. 21), *i.e.* when module R_1 is zero. Plain orthotropy is obtained when the two different anisotropic harmonics have same or opposite phases, *i.e.* $\Phi_0 - \Phi_1 = K\frac{\pi}{4}$, where $K = \{0, 1\}$ is the orthotropy shape parameter. A special case is distinguished when $R_0 = 0$, namely R_0-orthotropy [49]. A summary of the symmetry conditions is given in Table 2.

Elastic symmetry	Polar condition
Orthotropy	$\Phi_0 - \Phi_1 = K\frac{\pi}{4}, K \in \{0,1\}$
R_0-Orthotropy	$R_0 = 0$
Square Symmetry	$R_1 = 0$
Isotropy	$R_0 = R_1 = 0$

Table 2: Conditions for elastic symmetries in terms of polar invariants [21]

As we are interested in the bending stiffness behaviour of uncertain stacking sequences which can be elastically coupled, the polar formalism will be applied to the modified bending stiffness tensor $\tilde{\mathbf{D}}$ from Eq. (5). Its polar components are noted $T_0^{\tilde{D}}, T_1^{\tilde{D}}, R_0^{\tilde{D}}, R_1^{\tilde{D}}, \Phi_0^{\tilde{D}}, \Phi_1^{\tilde{D}}$, according to relations Eqs. (17) - (20).

Naturally, admissible values of such polar parameters are limited within a domain of existence satisfying thermodynamic constraints [25]. For composite laminates, there are additional constraints that originate in the layup geometry, which means angle values and their distribution throughout the thickness. Considering the case of nominally orthotropic laminates made of a given elementary layer or base material, the bounds are obtained in [26, 25] as

$$0 \leq R_0 \tag{27}$$

$$0 \leq R_1 \tag{28}$$

$$R_0 \leq R_0^{max} \tag{29}$$

$$2\left(\frac{R_1}{R_1^{max}}\right)^2 - 1 \leq (-1)^{K-K^{BM}}\left(\frac{R_0}{R_0^{max}}\right) \tag{30}$$

in terms of the anisotropic moduli R_0 and R_1 and the orthotropy-shape parameter K ($K = \{0,1\}$, see Table 2) of the in-plane or bending behaviour of the laminate, as well as of the orthotropy shape parameter K^{BM} of the base material of the constitutive orthotropic layer. We can distinguish Eqs. (27, 28) which have to be imposed because R_0 and R_1 are non-negative moduli (see Eqs. (17)) - (20)) from the specific geometric bounds expressed by Eqs. (29, 30). As shown in [25], the geometric constraints for composite laminates are always more restrictive than the thermodynamic constraints. Then, conditions Eqs. (27) - (30)) are sufficient to represent the boundaries of the admissible domain for all othotropic laminates made of a given base-material layer.

As already done in [24, 26], the polar module R_0 and the orthotropy-shape parameter K can be combined in a single parameter $R_K = (-1)^K R_0$, which is then a real-valued parameter with sign. We remind also that for any laminate made of identical layers (same base material and same thickness), the isotropic parameters of the laminate are fixed and equal to the ones of the base material (see for instance [24, 26]). Then, only two independent parameters $(-1)^K R_0$ and R_1 are sufficient to describe the behaviour of an orthotropic laminate made of a given base-material layer. A graphical representation of the polar domain is given in Fig. 3 in the case of a base material with $K^{BM} = 0$, which is the most common case encountered in structural applications of composite laminates.

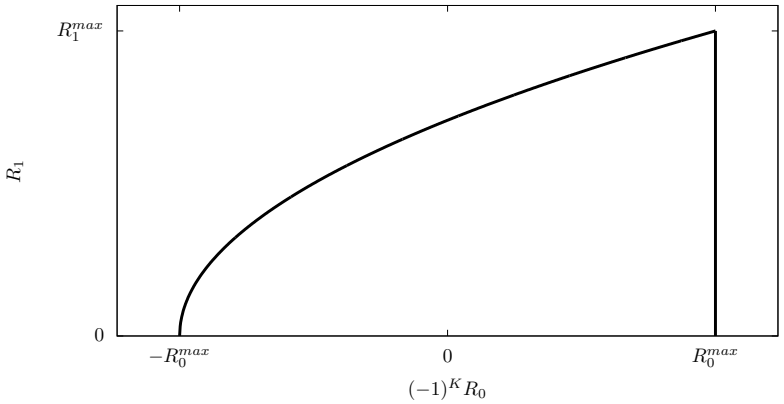

Figure 3: Domain for orthotropic laminates in the plane of the anisotropic polar parameters $(-1)^K R_0$ and R_1.

The stiffness behaviour of the laminate represents one of the main influences on the system presented in section 2. Changes in the laminate behaviour will alter the modal pattern and consequently the flutter response of the wing. The main uncertainties in composite laminates arise due to fibre placement errors and deviations in the ply thicknesses. Depending on the manufacturing method, the magnitude of these errors can vary, but a given range of tolerance affects all fabrication processes. These errors have in turn an effect on the stiffness properties, *i.e.* on the polar parameters of the laminate, which become random. However, with a random laminate, neither any material symmetry, nor uncoupling ($\mathbf{B} = \mathbf{0}$), nor any specific orthotropy direction, nor invariance of the isotropic components can be guaranteed. Consequently, the vector of random parameters considered consists of all the six polar components of the modified bending tensor $\tilde{\mathbf{D}}$, which has been introduced to reflect the influence of elastic coupling $\mathbf{B}$ (Eq. (5)).

$$\boldsymbol{\theta} = \{T_0^{\tilde{D}}, T_1^{\tilde{D}}, R_0^{\tilde{D}}, R_1^{\tilde{D}}, \Phi_0^{\tilde{D}}, \Phi_1^{\tilde{D}}\} \tag{31}$$

This number of parameters is significantly lower than the total number of ply angles and thicknesses in a typical laminate and stays constant independently of the number of layers in the laminate. However, this reduction in the number of parameters comes with the by-effect that the polar parameters Eq. (31) are correlated, which is a hard problem in uncerainty quantification. A solution approach will be shown in section 5. Before analysing the effect of uncertainties, we conduct a deterministic study of the aeroelastic response of the system introduced in section 2 over the polar domain of nominally orthotropic and uncoupled laminates.

4. Deterministic analysis of the aeroelastic response

In this section, a deterministic study will be performed on the flutter behaviour of composite wings following the layout presented in section 2. The flutter critical velocity and frequency will be analysed in terms of the variation of the polar constants over their admissible domain, thus obtaining the flutter response surface. Afterwards, specific points will be chosen in the admissible domain of orthotropic laminates and studied in detail.

Throughout this work, sixteen-layer layups based on AS4/3502 graphite/epoxy laminate [19, 50] will be studied. The engineering moduli of this base layer are shown in Table 3 along with

the ply thickness and the density of the material. The corresponding polar parameters are given in Table 4, as they can be deduced from Eqs. (17) - (20). Looking at the elastic modules of this base material, and particularly considering that the values for the anisotropic polar constants R_0 and R_1 are significantly different from zero, it can be concluded that the directional character of the base material is strong.

$E_1[GPa]$	$E_2[GPa]$	$G_{12}[GPa]$	$\nu_{12}[-]$	$\rho[kg/m^3]$	Ply thickness $t[mm]$
138.0	8.96	7.1	0.3	1600	0.1

Table 3: Material properties of AS4/3502 UD layer

$T_0^{\mathrm{BM}}[GPa]$	$T_1^{\mathrm{BM}}[GPa]$	$R_0^{\mathrm{BM}}[GPa]$	$R_1^{\mathrm{BM}}[GPa]$	$\Phi_0^{\mathrm{BM}}\,[^\circ]$	$\Phi_1^{\mathrm{BM}}\,[^\circ]$
21.35	19.15	14.25	16.23	0	0

Table 4: Polar constants for the stiffness tensor of the AS4/3502 UD layer (BM = Base Material)

We notice that if we consider nominally uncoupled laminates ($\mathbf{B} = \mathbf{0}$), the modified bending tensor $\tilde{\mathbf{D}}$ and the bending tensor $\mathbf{D}$ coincide, and so do their polar moduli.

Fig. 4 shows the admissible domain for the bending stiffness polar components $(-1)^K R_0^D$ and R_1^D of nominally orthotropic and uncoupled sixteen-layer layups that can be obtained using layers of AS4/3502 as base material. According to the Classical Laminated Plate Theory (CLPT) equations and to polar expressions Eq. (17) - (20), the nominal values of the isotropic polar bending components T_0^D and T_1^D for such laminates are fixed and can be obtained as follows (t is the layer thickness)

$$T_0^D = \frac{1}{3}\sum_{k=1}^{n_{\mathrm{plies}}} T_0^{\mathrm{BM}}\left(z_k^3 - z_{k-1}^3\right) = \frac{(n_{\mathrm{plies}}t)^3}{12} T_0^{\mathrm{BM}} \approx 7.29\mathrm{Nm} \tag{32}$$

$$T_1^D = \frac{1}{3}\sum_{k=1}^{n_{\mathrm{plies}}} T_1^{\mathrm{BM}}\left(z_k^3 - z_{k-1}^3\right) = \frac{(n_{\mathrm{plies}}t)^3}{12} T_1^{\mathrm{BM}} \approx 6.54\mathrm{Nm} \tag{33}$$

The anisotropic polar parameters $(-1)^K R_0^D$ and R_1^D of the nominal orthotropic layup have to satisfy the bounds in Eqs. (27) - (30) where $R_0^{D,max}$ and $R_1^{D,max}$ are

$$R_0^{D,max} = \frac{1}{3}\sum_{k=1}^{n_{\mathrm{plies}}} R_0^{\mathrm{BM}}\left(z_k^3 - z_{k-1}^3\right) = \frac{(n_{\mathrm{plies}}t)^3}{12} R_0^{\mathrm{BM}} \approx 4.86\mathrm{Nm} \tag{34}$$

$$R_1^{D,max} = \frac{1}{3}\sum_{k=1}^{n_{\mathrm{plies}}} R_1^{\mathrm{BM}}\left(z_k^3 - z_{k-1}^3\right) = \frac{(n_{\mathrm{plies}}t)^3}{12} R_1^{\mathrm{BM}} \approx 5.54\mathrm{Nm} \tag{35}$$

For each pair of values $\left\{(-1)^K R_0^D, R_1^D\right\}$ within the admissible domain, we evaluated the flutter response of the cantilevered wing as depicted in Fig. 1, with the geometric and aeromechanical parameters from Table 1, in order to obtain the response surface of flutter velocity and circular frequency shown in Fig. 4. In these calculations, the principal orthotropy axis of the laminate is considered to be aligned with the wing midchord axis x (i. e. $\Phi_1^D = 0$). We notice that the critical flutter velocity V_f cannot be tied to one parameter alone and that is also not sufficient to maximise

one or both of the parameters to achieve a high value for V_f, as the maximum for V_f in this particular plane is found at $\left\{(-1)^K R_0^D = -1.948, R_1^D = 3.032\right\}$ with a value of $V_f = 143.48 m/s$ (green square dot in Fig. 4). Furthermore, just starting out from the point of maximum V_f, we note an important step in V_f, which follows a straight line described approximately by the equation

$$\begin{bmatrix} (-1)^K R_0^{D,switch} \\ R_1^{D,switch} \end{bmatrix} = \begin{bmatrix} 0.92 \\ 0 \end{bmatrix} + s \begin{bmatrix} -2.87 \\ 3.03 \end{bmatrix}, s \in [0,1] \tag{36}$$

Exactly the same step is present in the frequency response surface in Fig. 4(b) and it splits the admissible domain into two sub-regions with values of frequency of about $850\,[rad/s]$ and $500\,[rad/s]$, respectively on the left and on the right side of the step. This is due to an abrupt change in the instability mechanism, which is a switch of the aeroelastic mode when passing through the step. Other than at the switching point, the frequency values stay almost constant in each of the two sub-regions of the domain. The flutter velocity response surface shows more evident changes. On the right of the step, the flutter velocity is almost insensitive to $R_1^{\tilde{D}}$, whereas the response surface is clearly inclined left of the step, showing a greater sensibility of V_f to $R_1^{\tilde{D}}$ in this part. The discontinuity is particularly important on V_f, as the minimum critical flutter velocity of $V_f = 76.3\,[m/s]$ as well as the maximum of $V_f = 143.48\,[m/s]$ occur in direct vicinity to the step.

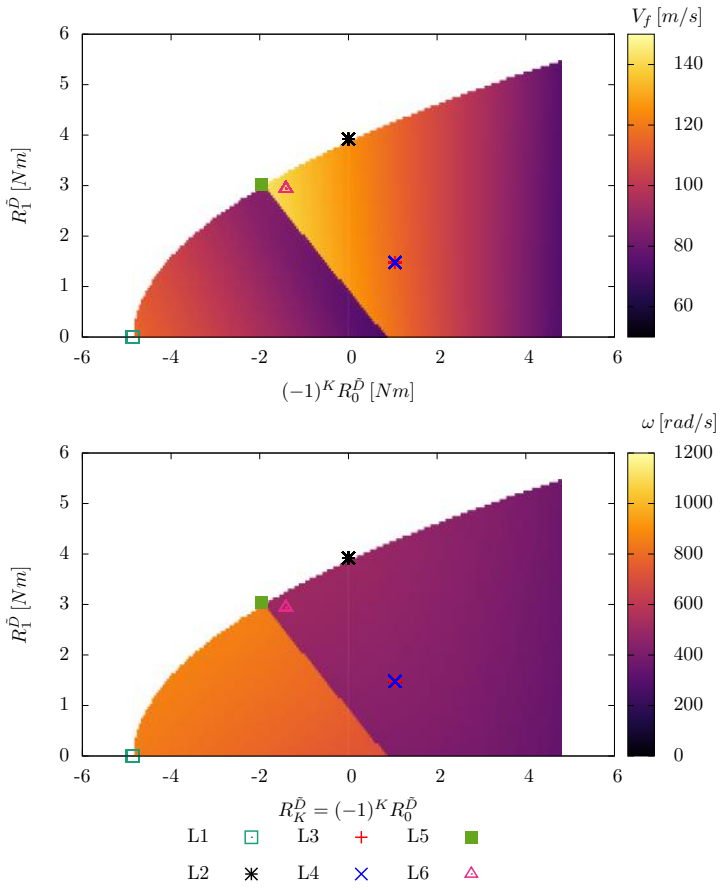

Figure 4: Response surface in critical flutter velocity V_f and flutter frequency ω in the R_K^D—R_1^D plane, for orthotropic layups based on AS4/3502 UD laminate

Based on the response surface presented in Fig. 4, six configurations are extracted to be examined separately in a stochastic framework when considering uncertainties on the constitutive parameters of the laminates (angles and thicknesses). Their locations in the orthotropic plane are indicated by the markers in Fig. 4 and their polar parameters are given in Table 5 along with their corresponding critical flutter velocity and flutter frequency.

Case	$T_0^{\tilde{D}}[Nm]$	$T_1^{\tilde{D}}[Nm]$	$(-1)^K R_0^{\tilde{D}}[Nm]$	$R_1^{\tilde{D}}[Nm]$	$\Phi_0^{\tilde{D}}[°]$	$\Phi_1^{\tilde{D}}[°]$	$V_f\,[m/s]$	$\omega_f\,\left[\frac{rad}{s}\right]$
L1	7.288	6.538	-4.865	0	$\pi/4$	0	115.46	847.14
L2	7.288	6.538	0	3.916	0	0	125.06	498.82
L3/L4	7.288	6.538	1.048	1.484	0	0	116.26	448.60
L5	7.288	6.538	-1.948	3.032	$\pi/4$	0	143.48	505.24
L6	7.288	6.538	-1.408	2.941	$\pi/4$	0	138.67	499.83

Table 5: Polar properties and flutter response of the six configurations chosen on the response surface of Fig. 4. Corresponding stacking sequences are given in Tab. 6

Stacking sequences corresponding to the six configurations of Table 5 are given in Table 6 (angles are referred to the reference axis x in our model, as described in section 2). All layups are designed to be nominally orthotropic and uncoupled ($\mathbf{B} = \mathbf{0}$), which means that $\tilde{\mathbf{D}} = \mathbf{D}$ in the nominal configuration (cf. Eq. (5)). However, this convenient property cannot be guaranteed if the layup is modified or disturbed by uncertainties.

Case	Stacking sequence	Property summary
L1	$[45_2, -45_4, 45_2, -45_2, 45_4, -45_2]$	nominally square symmetric ($R_1^{\tilde{D}} = 0$)
L2	$[22.5_2, -22.5_4, 22.5_2, -22.5_2, 22.5_4, -22.5_2]$	nominally R_0-orthotropic ($R_0^{\tilde{D}} = 0$)
L3	$[\pm 23.2, 90, -23.2, 90, 23.2_2, -23.2, 23.2, -23.2_2, 90, 23.2, 90, \pm 23.2]$	general orthotropic, far from the step
L4	$[0, \pm 58.8, 0, -58.8, 0_2, 58.8, 58.8, 0_2, -58.8, 0, \mp 58.8, 0]$	same nominal properties as L3
L5	$[28.4_2, -28.4_4, 28.4_2, -28.4_2, 28.4_4, -28.4_2]$	general orthotropic, $V_{f_{max}}$
L6	$[34, 0, -34_2, \pm 34, 34, 0_2, -34, \pm 34, 34_2, 0, -34]$	general orthotropic, close to discontinuity

Table 6: List of laminates based on AS4/3502 corresponding to selected points on the response surface of Fig. 4

The six laminate configurations are chosen to study the effects of uncertainties on their particular propierties in section 5. The precise goals of the studies are detailed in the following.

- Layups L1 and L2 are both angle-ply sequences and are chosen to examine the effect of material symmetry, with L1 being square-symmetric ($R_1^D = 0$) and L2 being R_0-orthotropic ($R_0^D = 0$) (see Table 5).
- L3 and L4 are two distinct three-orientation general orthotropic layups that share the same nominal material properties, *i.e.* they correspond to a same and single point in the domain of orthotropic laminates (see Fig. 4). They will serve to investigate the influence of differences in the stacking sequences on the stochastic analysis.
- L5 is an angle-ply laminate placed in direct vicinity of the mode switch and coincides with the maximum critical flutter velocity. It will demonstrate the effect of the mode switch in the stochastic analysis.
- Finally, L6 is a three-orientation generally orthotropic laminate corresponding to a point in the domain that can be affected by the mode switch since it is placed in its vicinity, even if not exactly on the line of discontinuity.

To provide for a better understanding of the elastic behaviour of the different layups in their nominal configurations, circular diagrams of their equivalent engineering bending moduli are given in Fig. 5, where $E(\delta)$ and $G(\delta)$ represent respectively the bending Young's modulus and the torsional modulus in a frame shifted by an angle δ with respect to the reference axis x. At $\delta = 0$ (horizontal axis in Fig. 5), the values of the bending modulus E_x and the torsional modulus G_{xy} in the reference frame of our model can be found (see section 2). We notice that the curves of $E(\delta)$ and $G(\delta)$ for layups L3 and L4 are superposed, since the two layups correspond to the same point on the polar domain (see Fig. 4). We find that layup L2 has the highest bending modulus E_x, followed by layups L3 and L4, and then in decreasing order of E_x one finds L6, L5 and, further away, L1.

The material with the highest torsional modulus G_{xy} is the square-symmetric laminate L1, which is the only one in the "high shear" region of the orthotropic domain. Note that the square-symmetry of L1 can very clearly be identified very clearly from the diagram of Young's modulus $E(\delta)$, whereas the R_0-orthotropy of L2 is very difficult to distinguish just from the diagram.

The layups L3 and L4 show a less directional behaviour. Their anisotropic polar moduli in Table 5 are smaller than for the other laminates and their torsional stiffness $G(\delta)$ takes the form of a rounded square. Laminates L5 and L6 are general orthotropic layups with typical "butterfly" modulus shapes in bending stiffness $E(\delta)$ and cross-shaped torsional modulus $G(\delta)$. Their respective stiffnesses E_x and G_{xy} in the reference axes are intermediate stages between L1 and L2.

In summary, although the anisotropic parameters are not linearly linked to the engineering moduli and cannot be tied to one modulus alone, torsional stiffness G_{xy} on the principal axes goes down with higher values for $(-1)^K R_0^{\tilde{D}}$ and bending stiffness E_x in the reference axis of the wing goes up with higher values of $R_0^{\tilde{D}}$ and $R_1^{\tilde{D}}$.

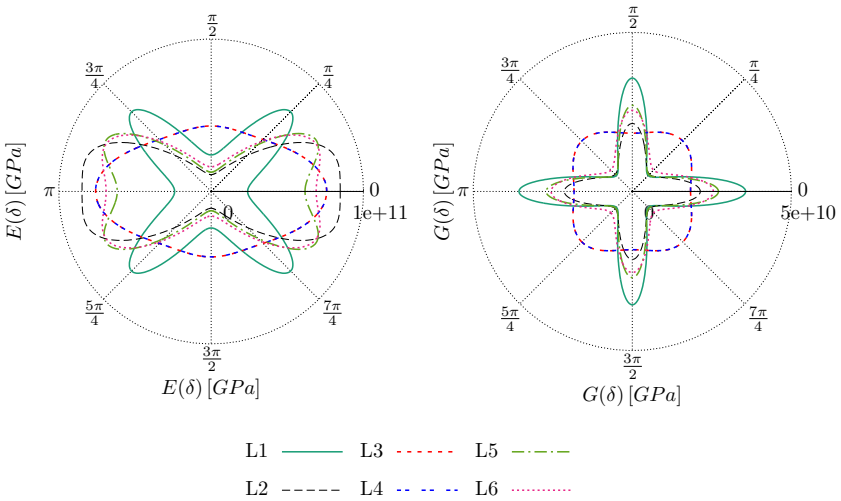

Figure 5: Circular diagrams of the nominal elastic moduli of the selected points of Table 5 and layups in Table 6.

Fig. 6 shows the aeroelastic $V-\lambda$ diagram for laminate L1 computed as explained in section 2. The critical flutter velocity of $V_f = 115.46\,[m/s]$ is indicated by the vertical bar in Fig. 6(a). From the mode shape in Fig. 6(b), one can clearly see that the flutter mode is bending-dominated and can be described as a second bending mode. The torsion component in the mode, although perceptible, is weak. This is in accordance with the high torsional stiffness G_{xy} and the weak bending stiffness E_x of layup L1.

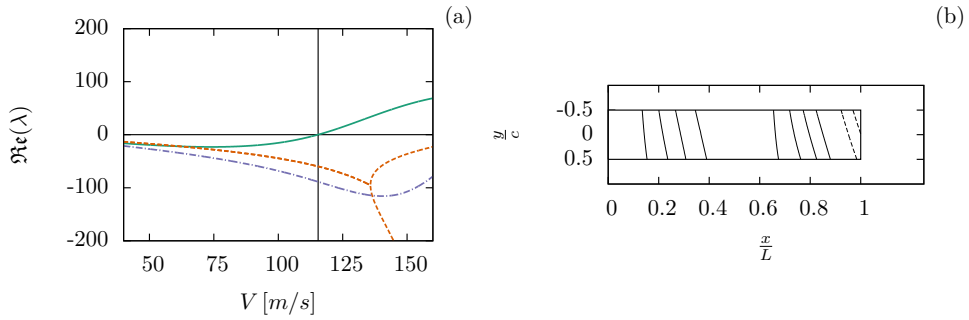

Figure 6: $V - \lambda$ flutter diagram and modal response of the square-symmetric L1 laminate. The vertical bar indicates the critical flutter velocity $V_f = 115.46\,[m/s]$.

Layup L2 shows a very different aeroelastic behaviour (see Fig. 7), since its bending stiffness E_x is much higher than for L1, while its torsional stiffness G_{xy} is substantially lower. Thus, its modal behaviour appears to be torsion-dominated, even if a weak bending component is present, but much less distinctive than in the L1 case. Also its critical flutter velocity is higher than for L1 ($V_f = 125.06\,[m/s]$).

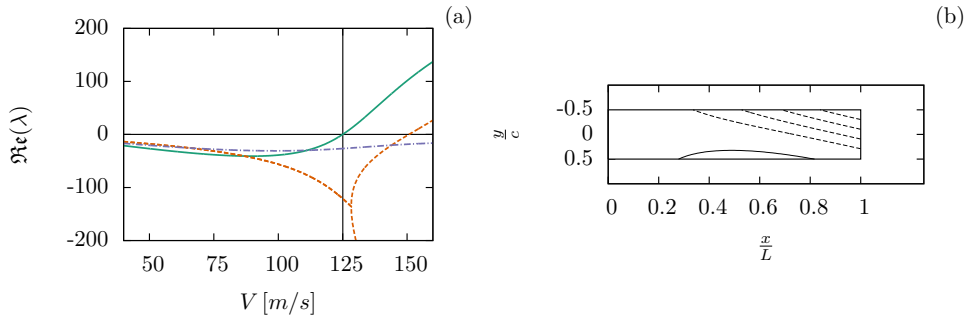

Figure 7: $V - \lambda$ flutter diagram and modal response of the R_0-orthotropic L2 laminate. The cricital flutter velocity $V_f = 125.06\,[m/s]$ is again indicated by the black bar.

The two distinct unstable modes of laminates L1 and L2 describe the two flutter regimes appearing on each side of the discontinuity on the response surface shown in Fig. 4. Now, we focus attention on layup L5, which is placed on the high-velocity limit of the switch (see green square dot in Fig. 4 and Table 6). In order to study the transition between the two regimes, we generate two offset configurations $L5^+$ and $L5^-$ by changing the lamination angle to $28.4° \pm 2°$, respectively. These offset configurations are still angle-ply laminates, thus they belong to the upper border of the flutter domain and they lay on the left and right side of the discontinuity in the aeroelastic response.

The flutter response of layup $L5^+$ is shown in Fig. 8. Its modal behaviour is essentially the same as for L1, *i.e.* it is characterised as a second bending mode. The unstable mode is shown by the dash-dotted violet line in the $V - \lambda$ flutter diagram in Fig. 8(a). Nevertheless, the real part of λ, representing a growth rate, does not pass the zero line by much and decreases again at higher velocities. This means that the mode would become stable again for airspeeds higher than about $130[m/s]$.

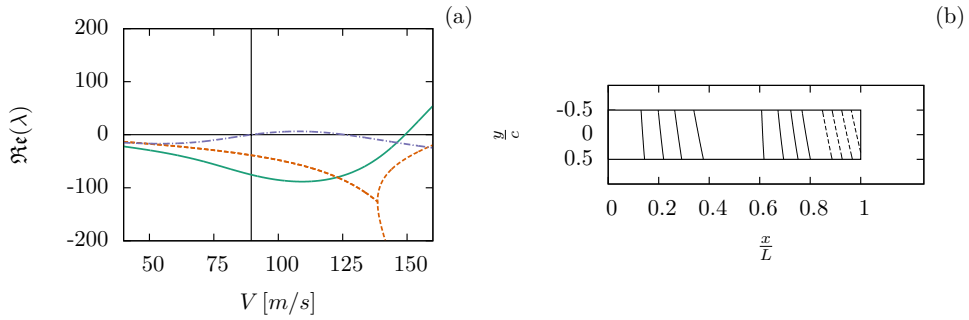

Figure 8: $V-\lambda$ flutter diagram and modal response of laminate L5$^+$. The cricital flutter velocity $V_f = 89.54\,[m/s]$ is indicated by the black bar.

When passing on to laminate L5$^-$, the mode that fluttered in the previous configuration, again represented by a violet dash-dotted line in the $V-\lambda$ diagram in Fig. 9(a), can still be recognised. However, it is no longer unstable, which can be attributed to the shift in the laminate sequence. The new flutter mode found in laminate L5$^-$ is shown by the solid green line. It could already be distinguished in the previous example (see the solid green line in Fig. 8(a)), but was not considered critical because it became unstable at higher velocities than the first mode.

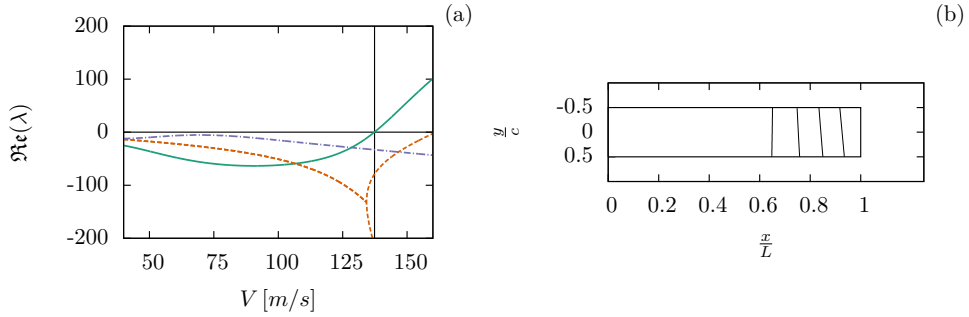

Figure 9: $V-\lambda$ flutter diagram and modal response of laminate L5$^-$. The vertical bar indicates the critical flutter velocity $V_f = 137.37\,[m/s]$.

The mode switch is thus caused by (de-)stabilisation of one of the aeroelastic modes as a function of the balance between the bending and torsional stiffness of the the composite laminate of the wing. The small increase in bending stiffness when passing from layup L5$^+$ to L5$^-$ stabilizes the second bending mode. However, the transition in mode shape is not directly to a torsion-dominated mode as found in layup L2 (see Fig. 7(b)), but resembles more a first bending mode (Fig. 9(b)), which is consistent with the increase in bending stiffness. In order to attain torsion-dominated modes, one has to move further right on the domain, where bending stiffness further increases and torsional stiffness decreases, as for laminate L2. This transition from bending- to torsion-dominated modes is smooth. The strong deviations of modal behaviour as a function of the material stiffness and anisotropy and the associated deviations in critical flutter velocity clearly highlight the need for uncertainty quantification. This is especially true in presence of mode switches, which create steps in the velocity response, meaning that even very small deviations in the material behaviour can cause violent changes in critical flutter velocity.

5. Uncertainty propagation

In this section, uncertainty quantification in ply angles and thicknesses is performed in order to study the stochastic aeroelastic response of the composite laminated wing previously investigated from a deterministic point of view. First, the considered parametric uncertainties are depicted. Next the stochastic solver developed to propagate the uncertainties in ply thicknesses and angles is briefly described. Then, the stochastic aeroelastic response is analysed for a selection of polar properties describing several laminates based on AS4/3502.

5.1. Uncertainty modeling

In this work, we consider the case of prefabricated layers of the size of the plate that are placed on top of each other, which is a common manufacturing method for small plates [51]. In that case, it is assumed that inside an individual layer, the ply angle is relatively constant, but deviations are due to the manual manufacturing process of layering the plies. This allows to the stochastic analysis of the laminate configurations L1 to L6 in Table 6 by considering random modeling of the ply angle to a single scalar random variable for each ply as in [18]. We remind that these layups correspond to five points, which were selected on the polar domain of Fig. 4 in order to study the effect of elastic symmetries (L1 and L2), of different stacking sequences (L3 and L4) and of mode switch on the aeroelastic response (L5 and L6), as explained in detail in section 4.

Hereafter, all ply angles and thicknesses are considered as uncertain variables characterised by a Gaussian distribution with standard deviation of $1\,[^\circ]$ and $0.005\,[mm]$ respectively, as reported in Table 7.

$\sigma_t[mm]$	0.005	$\sigma_\theta[^\circ]$	1.0

Table 7: Standard deviations of the uncertainties in ply thicknesses and angles characterised by Gaussian distributions

In order to compute the stochastic critical flutter velocity for a given layup configuration, we need to propagate uncertainties in ply angles and thicknesses. Unfortunately, even in the case of our rather simple aeroelastic model (see section 2), the use of plain Monte Carlo simulation is computationally costly. This is why it is desirable to consider accelerated stochastic methods such as polynomial-chaos approaches [29, 36]. Unfortunately, the number of uncertain constitutive parameters, ply angles and thicknesses, of a laminated plate equals $2n_{\text{plies}}$. In the studied case, $n_{\text{plies}} = 16$, so we would already attain 32 uncertain variables, which is not affordable for polynomial-chaos techniques due to the curse of dimensionality.

In the present work, we choose to consider the laminate's modified bending polar parameters, *i.e.* the vector $\boldsymbol{\theta}$ of Eq. (31), as stochastic variables. The advantage of this choice is to bring the number of uncertain parameters down to six independently of the number of constitutive layers in the laminate, even when dealing with coupled and non-symmetric stacking sequences. In order to measure how these uncertainties affect the stiffness properties and particularly the deviation from the nominal values and symmetries, plain Monte Carlo simulations are performed. For a given layup configuration, a set of 10^5 samples is considered according to the uncertainties in ply angles and thicknesses defined in Table 7. Fig. 10 shows the resulting scatter plots of the modified bending polar parameters $\boldsymbol{\theta}$ in the case of layup L5. The distributions of the anisotropic parameters exhibit rather strong correlation with the isotropic parameters, which indicates a big influence of the thickness uncertainty. On the contrary, the anisotropic components do not show very strong correlation with respect to each other. However, it must be noticed that the correlation pattern depends on the layup.

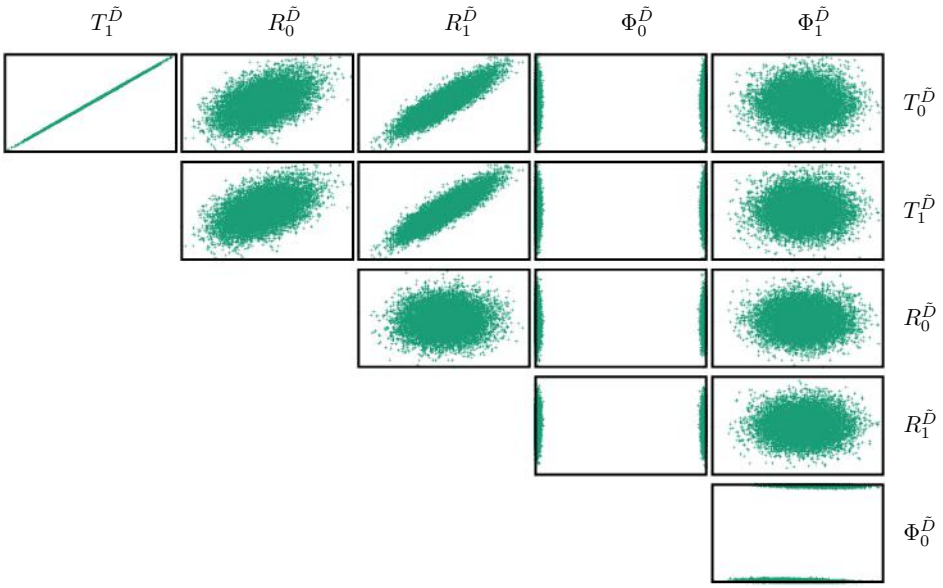

Figure 10: Scatter plots of pairs of modified bending polar parameters for layup L5 (10^5 samples drawn using Monte Carlo simulation).

5.2. Non-intrusive stochastic solver

In the present work, an arbitrary Polynomial-Chaos (aPC) spectral decomposition method [37] is specially adapted to deal with the correlation between the polar parameters. Indeed, the aPC method can deal with arbitrary forms of the measure of probability by numerically constructing the polynomials using the Gram-Schmidt algorithm [52]. The aPC expansion is more general than the generalized Polynomial Chaos method (gPC) [29] since it may deal with arbitrary distributions which can be described analytically or numerically [53] and with correlated random variables [54].

However, polynomial-chaos approaches cannot directly deal with discontinuous response surfaces. For this reason, we developed machine-learning techniques in order to identify the presence of discontinuities as well as to classify clusters of points belonging to separate regions of the response surface on either side of the discontinuity. Once the clusters are identified, the aPC method can be applied separately on each cluster in order to reconstruct the corresponding smooth region of the response surface. By employing machine-learning techniques we are able to treat the discontinuity in a proper and automatic way. The aPC method as well as the techniques of machine learning that we developed are described in detail in Appendix A.

In the following, we deploy the strategy of uncertainty quantification based on the combination of aPC and machine-learning techniques to the list of laminate sequences given in Table 6. In our study, we needed 10^3 samples of V_f and ω_f in order to reliably get converged solutions out of the step of machine learning, as well as to fit the response surface in the polynomial-chaos approach, thus reducing of 10^2 times the number of calls to the aeroelastic solver with respect to plain Monte Carlo techniques. In order to apply the aPC method, we conduct a preliminary sampling, by generating samples of $\tilde{D}$ which are propagated through the deterministic aeroelastic solver. These samples are then used for the fitting of the response surface as described in Appendix A. All results presented in the following were obtained using polynomials of order $P = 3$ in the aPC expansion.

5.3. Square-symmetric layup L1

Histograms in Fig. 11 describe the distributions of the polar parameters of modified bending stiffness (vector $\boldsymbol{\theta}$) for laminate L1 (refer to Fig. 4 and Tables 5 and 6) when applying fabrication errors on angles and thicknesses according to data in Table 7.

The distributions of the isotropic polar parameters mainly depend on the thicknesses. As the $\mathbf{D}$ bending stiffness tensor is function on the cubes of the ply limits z_k (see eq. 32), which are basically sums of the Gaussian distributed thicknesses, the distribution of its polar parameters is dominated by a normal distribution to the cube. The curves have their maximum at around the nominal value (vertical arrows in Fig. 11) and are steeper than a simple normal distribution, as can be seen in Fig. 11(a) and 11(b).

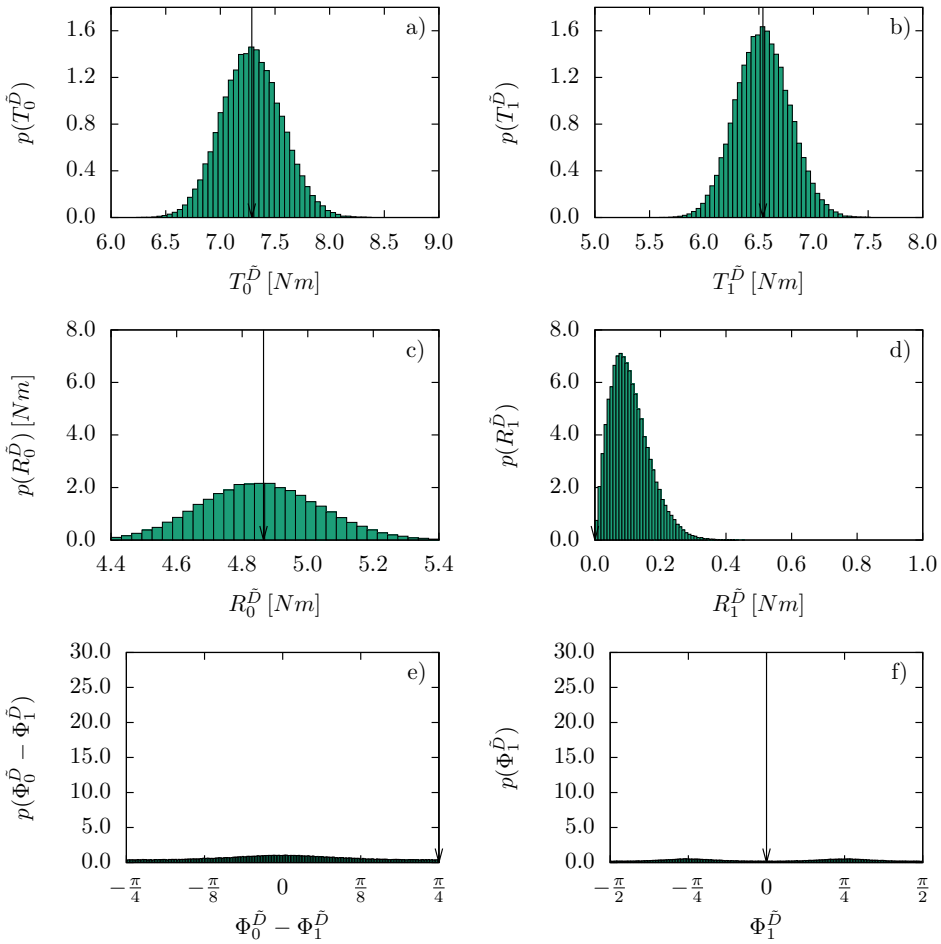

Figure 11: Distribution of the modified bending polar parameters for laminate L1 (cf. Table 6) due to the uncertainties in ply angles and thickness described in Table 7 obtained by 10^5 Monte Carlo draws. Vertical arrows point the nominal values of the bending polar parameters for layup L1.

As the nominal value of $T_0^{\tilde{D}}$ is higher than the nominal $T_1^{\tilde{D}}$, its distribution is more widely spread. The same behaviour can be observed for the isotropic components in the case of layups L2 to L6, so the corresponding distributions will not be commented further in the following subsections.

The modified bending stiffness tensor $\tilde{\mathbf{D}}$ (see Eq. (5)) takes into account the membrane-bending coupling that arises when the nominal stacking sequences are perturbed by fabrication errors. Its isotropic components are consequently not completely independent from the ply angle uncertainties, which create a slight downshift in the parameter distribution. However, this barely manifests in the shown histograms. An additional discussion on the separate effect of uncertainties in angles and thicknesses on the distributions of polar parameters can be found in [55].

Naturally, the influence of the ply angle uncertainty is much higher in the anisotropic components of the polar parameters of the material. Most importantly, the property of square-symmetry is lost, as $R_1^{\tilde{D}}$ shifts up from its nominal zero value. However, the values of $R_1^{\tilde{D}}$ stay low, which means that the $R_1^{\tilde{D}}$ characteristics are not very distinct (Fig. 11(d)). This goes along with the associated angle distribution being very widely spread: the direction of the axis of orthotropy $\Phi_1^{\tilde{D}}$, which was undefined in the nominal square-symmetric case, shifts to $\pm\frac{\pi}{4}$ (Fig. 11(f)). The direction of the square symmetry stays in the same phase as before, so $\Phi_0^{\tilde{D}} - \Phi_1^{\tilde{D}}$ recenters around 0 (Fig. 11(e). Modulus $R_0^{\tilde{D}}$ becomes widely spread under both the influence of the ply angle and thickness uncertainties (Fig. 11(c)). The slight downshift with respect to the nominal value is probably due to the ply angle uncertainty.

It must be noticed that, even if one assumes Gaussian distributions of angles and thicknesses, the distributions of the bending polar parameters are not Gaussian anymore. Instead, they can be arbitrary symmetric or skew distributions, as it is evident in the case of modulus $R_1^{\tilde{D}}$ (see for instance Fig. 11). This result is confirmed in the case of layups L2-L6 (see for instance Fig. 13(c)), which are described in the following subsections.

Now, the distribution of the critical flutter velocity V_f is calculated by the aPC method by direct propagation of the stochastic polar parameters of vector $\boldsymbol{\theta}$ and is given in Fig. 12. It has a bell shape with the highest probability density around the nominal value, which is pointed by the thick black arrow in the figure. While of course the deviations are noticeable, the distribution remains relatively narrow. As the aeroelastic behaviour is dominated by the anisotropy, this can be attributed to the fact that the response surface depicted in Fig. 4 does not exhibit high gradients in the region around the nominal point for L1.

The classical flutter margin, which is just a plain 15% offset from the nominal value (see the dash-dotted red arrow in Fig. 12), thus seems exaggerated in this case. It is situated far below any region with significant probability density. A comparison with an estimation of the 1% percentile (dashed blue line in the figure) shows a large offset, suggesting some margin for aeroelastic optimisation.

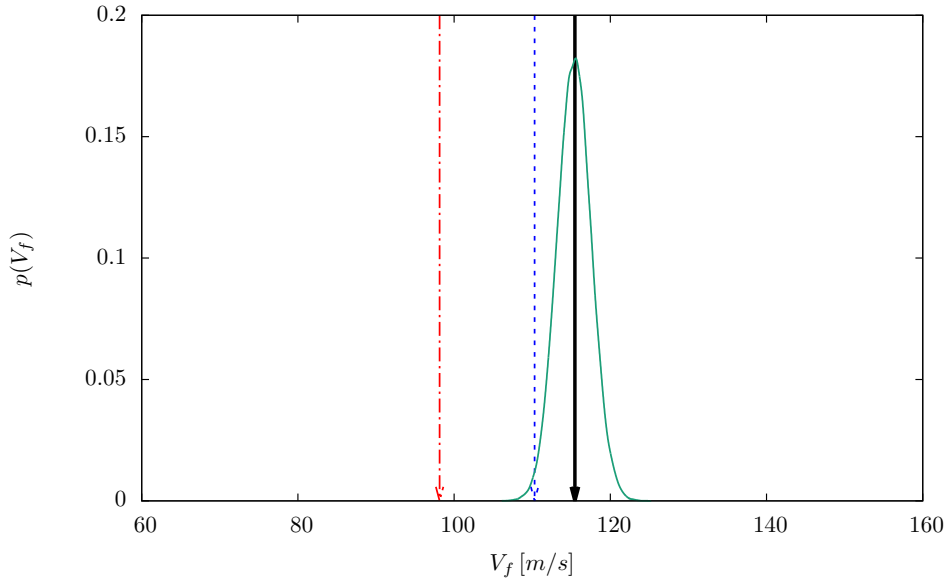

Figure 12: Probability density function of V_f for the square-symmetric laminate L1 obtained by the aPC method (with $P = 3$) based on the uncertain parameter input of Table 7. The solid black arrow indicates the nominal critical flutter speed, the red dash-dotted arrow is the classical 15% flutter margin and the blue dashed arrow indicates the 1% percentile for the occurrence of flutter.

5.4. R_0-orthotropic layup L2

Layup L2 represents another special case of elastic symmetry [49], being $R_0 = 0$ in the nominal configuration (see Table 5). The nominal stacking sequence is given in Table 6 and the representative point is illustrated in Fig. 4. The stochastic behaviour changes accordingly. Histograms in Fig. 13 represent distributions of the modified bending polar parameters for laminate L2 obtained by Monte Carlo simulation. With respect to the previous, square-symmetric example, the behaviour of the anisotropic components is flipped. $R_0^{\tilde{D}}$ deviates up from its nominal zero value and shows a skew distribution (see Fig. 13(c)), being zero a limit value for modulus $R_0^{\tilde{D}}$. Correspondingly, in Fig. 13(e) one can observe a large variability in the stochastic polar parameters, according to the widely spread distribution of the difference of polar angles $\Phi_0^{\tilde{D}} - \Phi_1^{\tilde{D}}$ with a bi-modal shape equally distributed between $0\,[rad]$ and $\pm\frac{\pi}{4}\,[rad]$. As a matter of fact, the polar angle $\Phi_0^{\tilde{D}}$ is not defined in the nominal configuration being $R_0^{\tilde{D}} = 0$, and the uncertainties on ply angles and thicknesses make the laminate deviate from the property of R_0-orthotropy and oscillate between *low-* and *high-shear* orthotropy (respectively, on the right and left side of the polar domain, where the orthotropy shape parameter is $K^{\tilde{D}} = 0$ or $K^{\tilde{D}} = 1$).

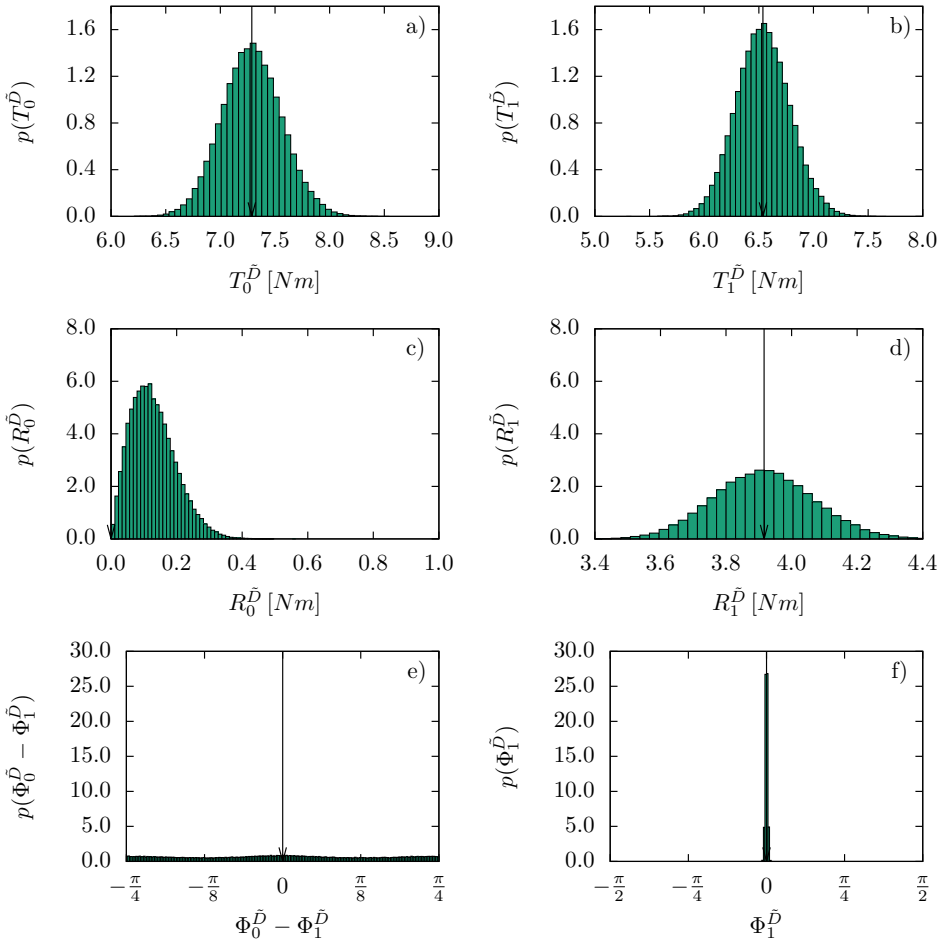

Figure 13: Distribution of polar parameters for the R_0-orthotropic laminate L2 (cf. Table 6) due to the uncertainties in ply angles and thickness described in Table 7.

The $R_1^{\tilde{D}}$ modulus is also highly uncertain, as can be noticed in the rather widely spread distribution in Fig. 13(d). In contrast, the corresponding angle $\Phi_1^{\tilde{D}}$ has a very narrow distribution (see Fig. 13(f)), which means that the principal stiffness direction does not deviate that much from its nominal position.

Figure 14 presents the flutter velocity distribution for configuration L2 obtained by propagating the uncertain polar parameters in Fig. 13 through the aPC stochastic surrogate model. It presents a steep bell shape with the probability density maximum very close to the nominal value (black solid arrow in the figure). This distribution is similar in shape but wider than the one for the square-symmetric layup L1 (cfr. Fig. 12). This can be attributed to the response surface being steeper around the nominal point for layup L2 (cfr. Fig. 4), rather than to a particular deviation in the polar parameters. Despite the higher uncertainty in the distribution, the classical flutter margin (dashed red arrow in Fig. 14) is still quite far off any region of noticeable probability density. Again, the offset to the 1% percentile (blue dashdotted line in the figure) is high, suggesting optimisation potential.

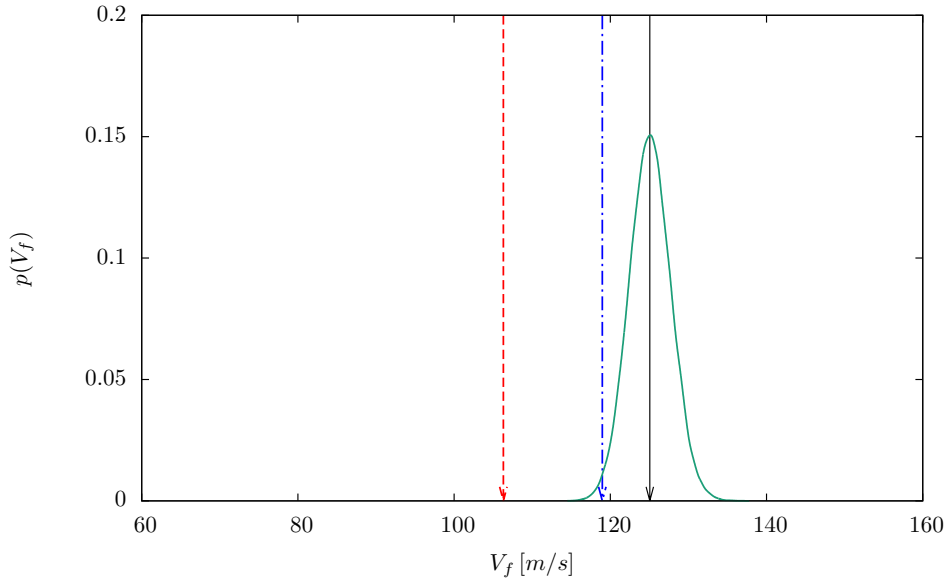

Figure 14: Probability density function of V_f for R_0-orthotropic laminate L2 obtained by the aPC method (with $P = 3$) based on the uncertain parameter input of Table 7. The solid black arrow indicates the nominal critical flutter speed, the red dashed arrow is the classical 15% flutter margin and the blue dash-dotted arrow indicates the 1% percentile for the occurrence of flutter.

5.5. Influence of the layup sequence on uncertainties

As it can be noticed in the previous subsections, the uncertainties in the polar parameters change with the base configuration. In this subsection, advantage is taken of the possibility to design layups with the same nominal stiffness properties, which was done here for layups L3 and L4 (cfr. Tables 5 and 6, as well as Fig. 4). This allows to isolate layup effects in the distributions. Histograms of the modified bending polar parameters for layups L3 and L4 are obtained by Monte Carlo simulation and are shown in Fig. 15. The solid green and dashed orange lines refer to L3 and L4 respectively. Other than L1 and L2, laminates L3 and L4 are general orthotropic three-orientation layups and they are not situated on the boundary of the polar domain. Consequently, the distributions of the anisotropic moduli in Fig. 15(c)-(d) are more symmetric and narrower than observed in the previous cases. Neither significant up- or downshift of the main probability density mass from their nominal value can be observed. Moreover, as both anisotropic components have nominal non-zero values, polar angles are quite well determined, as one can see from the narrow distributions in Fig. 15(e)-(f).

Comparing the distributions of the two layups L3 and L4, differences can be observed notably in the $R_0^{\tilde{D}}$ component and the associated angle (Fig. 15(c) and 15(e)). The distribution of $R_0^{\tilde{D}}$ for L3 is flatter and has longer tails than its L4 counterpart. In contrast, the distribution for the associated angle $\Phi_0^{\tilde{D}}$ is narrower with a higher peak. This is consistent with the previous observation that a higher uncertainty in the modulus compensates for a lower uncertainty in the polar angle, and *vice versa*.

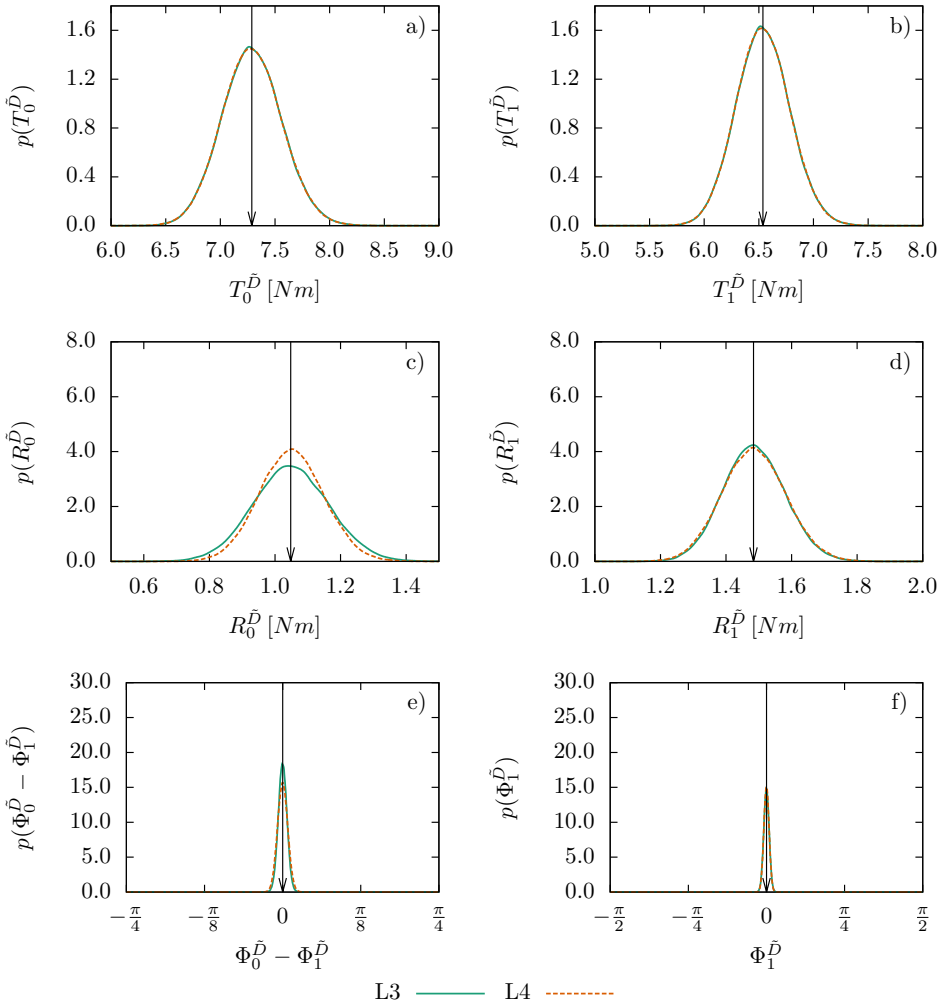

Figure 15: Distributions of the polar parameters for layups L3 and L4 (cf. Table 6) due to the uncertainties in ply angles and thickness described in Table 7 (solid green line for L3 and dashed orange line for L4).

Despite the difference in the distributions of their polar parameters, the distributions in critical flutter velocity obtained by the aPC procedure are virtually the same for L3 and L4, as shown in Fig. 16 by the solid green and dashed orange line respectively. Any differences cannot reliably be distinguished from numerical errors. Again, the curves are bell-shaped, with a spread similar to the spread of the R_0-orthotropic example (see previous subsection). As they have the same nominal polar parameters, they share the same nominal value of V_f (black solid arrow in the figure) and thus the same 15% flutter margin (red dashed line in the figure). The percentiles are almost the same and they are represented by the blue dash-dotted arrow in Fig. 16. As in the case of layups L1 and L2, the downshift of the 15% flutter margin with respect to the probability distribution of flutter velocity suggests that the stochastic aeroelastic response could be improved in a robust optimisation framework.

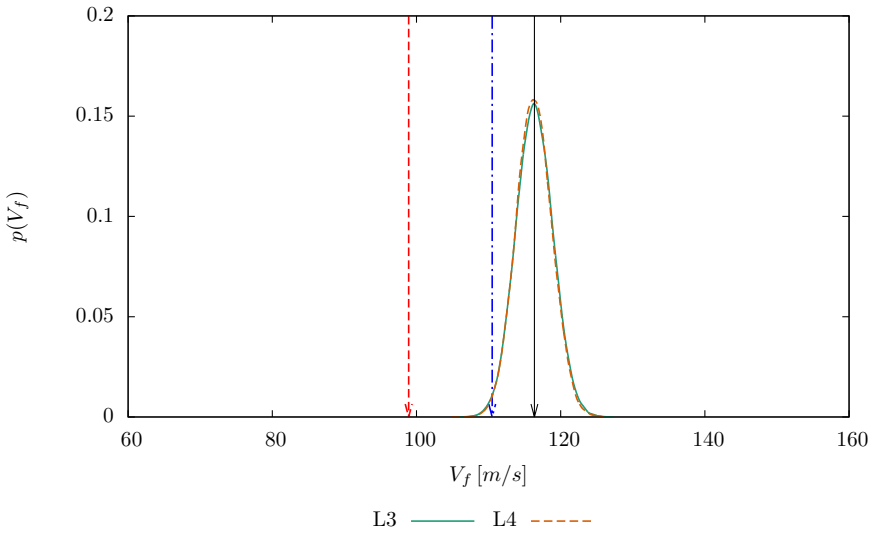

Figure 16: Probability density functions of V_f for the two general orthotropic layups L3 and L4 (solid green and dashed orange lines, respectively) obtained by the aPC method (with $P = 3$) based on the uncertain parameter input of Table 7. The solid black arrow indicates the nominal critical flutter speed, the red dashed arrow is the classical 15% flutter margin and the blue dash-dotted arrow indicates the 1% percentile for the occurrence of flutter.

5.6. Optimal configuration and mode switch

We study now configurations which are affected by the mode switch observed in section 4 and visible in Fig. 4. The first configuration corresponds to layup L5, which is located at the optimum in terms of critical flutter velocity in the orthotropic plane (cfr. Fig. 4 and Tables 5 and 6 for the description of the nominal configuration). Polar moduli $R_0^{\tilde{D}}$ and $R_1^{\tilde{D}}$ being non-zero in the nominal configuration, their distributions in Figs. 17(c)-(d) are bell-shaped with the maximum probability density well centered around their nominal values. However, in both cases the upper tail of the distribution seems to be slightly longer. The distribution for the principal stiffness direction $\Phi_1^{\tilde{D}}$ is centered around $0\,[rad]$ and very peaked (see Fig. 17(f)), while the offset distribution of $\Phi_0^{\tilde{D}} - \Phi_1^{\tilde{D}}$ is distributed at the $\frac{\pi}{4}$ limits (see Fig. 17(e)). The split in the angular difference distribution is only a graphical effect; the angles being periodic, values $\pm\frac{\pi}{4}$ correspond to the same orthotropic shape and the distribution in Fig. 17(e) is centered on the nominal value of the difference $\Phi_0^{\tilde{D}} - \Phi_1^{\tilde{D}}$.

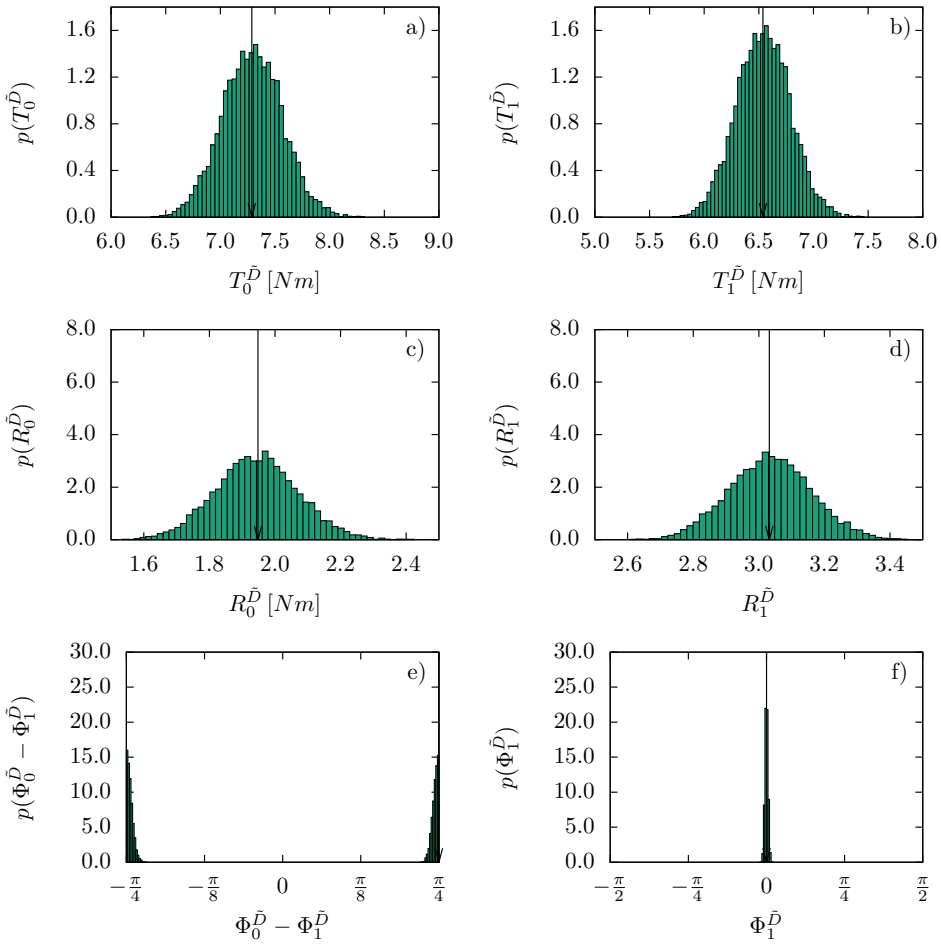

Figure 17: Distributions of the polar parameters for layup L5 (cf. Table 6) obtained by Monte Carlo simulation based on the uncertainties in ply angles and thickness described in Table 7.

The distribution of the critical flutter velocity V_f for laminate L5 is obtained by combination of aPC and machine-learning techniques (refer to Appendix A for a detailed description) and the result is depicted in Fig. 18.

Based on the previously shown uncertain polar parameters laminate L5, Figure 18 shows the corresponding distribution of the critical flutter velocity V_f. It clearly shows that the mode switch is triggered for the configuration at study by fabrication errors on ply angles and thicknesses. In fact, the distribution has a bimodal shape with one peak which is centered on the nominal value of V_f (black solid arrow in the figure), and a second peak located at lower values of flow velocity (roughly in the interval $[70, 100]\,[m/s]$). The individual bumps have a higher spread than the distributions shown for laminates L1-L4, so not only the level of uncertainty is augmented by the presence of the mode switch, but also the deviations inside the modes appear to be more important, which is due to the relatively steep and complex behaviour of the response surface in the vicinity of the discontinuity. We can notice that the discontinuity in the critical flutter velocity arises even if the random polar parameters are continuous as it is shown in Fig. 10. Instead, the changes in the stiffness properties cause the mode switch as explained at the end of Section 4.

In this configuration, it is clear that the classical flutter margin (-15% with respect to the nominal value of V_f, pointed by the red dashed arrow in Fig. 18) is well above the first peak of probability density situated at lower values of V_f. This is also very clearly demonstrated by the 1% percentile marker (blue dash-dotted arrow in Fig. 18), which is more than $40\,[m/s]$ below the classical flutter margin. The stochastic analysis can add security for flutter calculations in this scenario.

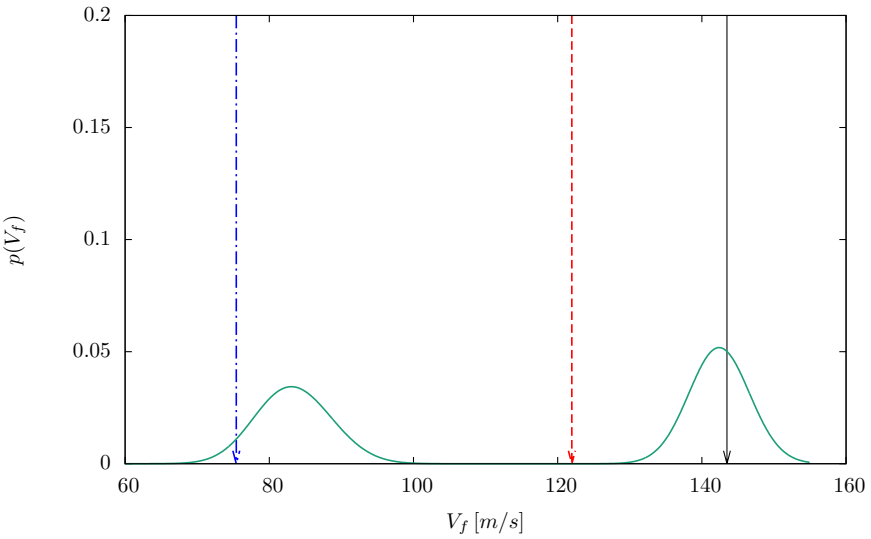

Figure 18: Probability density function of V_f for the optimal angle-ply laminate L5 obtained by the aPC method (with $P = 3$) and machine-learning techniques based on the uncertain parameter input of Table 7. The solid black arrow indicates the nominal critical flutter speed, the red dashed arrow is the classical 15% flutter margin and the blue dash-dotted arrow indicates the 1% percentile for the occurrence of flutter.

5.7. Offset from the mode switch

Finally, layup L6 is an example of a laminate affected by the mode switch, but not situated in the direct vicinity of the discontunuity. Furthermore, as in the case of L3 and L4, L6 is an additional example of a sequence which is not on the border of the admissible domain of

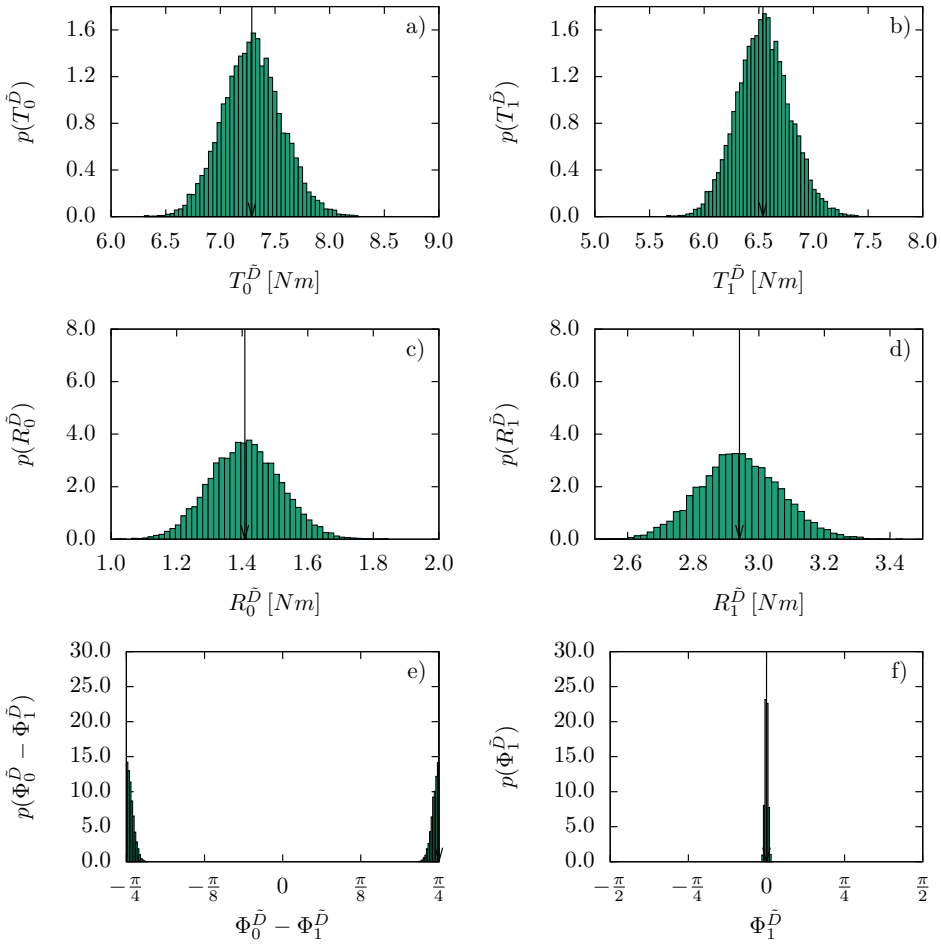

Figure 19: Distributions of the polar parameters for layup L6 (cf. Table 6) due to the uncertainties in ply angles and thickness described in Table 7.

orthotropic laminates and, in particular, it is not a plain angle-ply sequence, but a three-orientation $0/\pm\alpha$ laminate (with $\alpha = 34°$, see Table 6). We can remark that, keeping the same sequence, the point which is directly on the mode switch corresponds to the laminate with $\alpha = 35.6°$. This means that the angular offset of laminate L6 from the discontinuity is $1.6°$, which is higher than the standard deviation in the error distribution of ply angles (see Table 7).

Concerning the distribution of polar parameters, laminate L6 is very close to L5 in the polar domain, differing mostly in the nominal value of $R_0^{\tilde{D}}$ being lower than for L5 (see Fig. 19.c). The distributions of polar parameters $R_0^{\tilde{D}}$ and $R_1^{\tilde{D}}$ (see Fig. 19(c)-(d)) do not change much in shape with respect to the previous case. The distributions are bell shaped, with the main probability density mass distributed around the nominal values and a slight accent on the upper tail. The distributions of the associated angles stay narrow (see Fig. 19(e)-(f)).

Even if the fabrication errors defined in Table 7 are limited in spread, they still trigger the mode switch for layup L6. The corresponding distribution of the critical flutter velocity V_f is given in Fig. 20 and it shows a bimodal shape, with one bump in the probability density much less peaked compared to the L5 case. However, the main bump in Fig. 20 does not get narrower in spread by much, although it gets much steeper. This indicates once more that the uncertainty

is mainly linked to the modal behaviour and the mode associated to the higher flutter velocities just receives more samples in this case. Due to the second bump in probability density in the low-velocity region, the estimate of the 1% quantile (blue dash-dotted arrow in Fig. 20) for the critical flutter velocity is well below the classical flutter margin (red dashed arrow in the figure). This indicates that the classical margin does not provide safety against flutter in all relevant configurations.

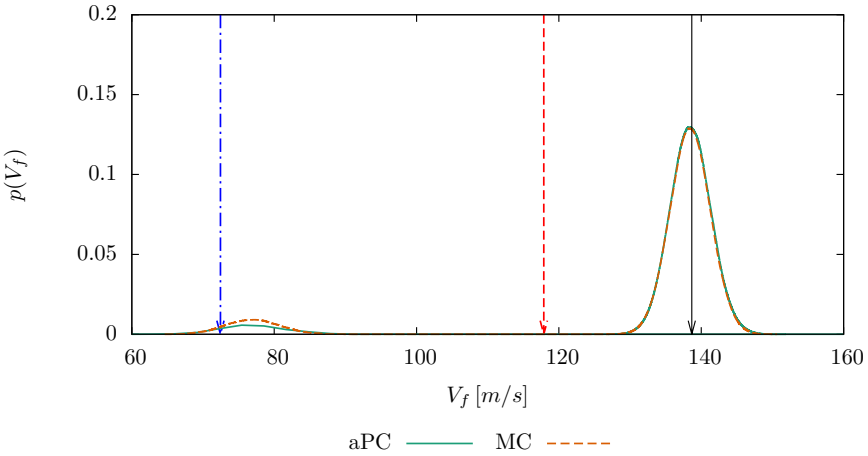

Figure 20: Probability density function of V_f for laminate L6 obtained by the aPC method (with $P = 3$) based on the uncertain parameter input of Table 7. The solid black arrow indicates the nominal critical flutter speed, the red dashed arrow is the classical 15% flutter margin and the blue dash-dotted arrow indicates the 1% percentile for the occurrence of flutter.

6. Conclusion

In this work, uncertainty propagation in both ply thickness and angular fibre placement of composite laminates was performed to quantify their effects on the critical flutter velocity of a rectangular straight cantilevered plate wing, consisting of sixteen composite plies. In contrast to previous works, a combined study of both uncertainties was carried out without imposing restrictions on the resulting laminate behaviour, thus fully reflecting the consequences of random deviations.

Analysis was enabled by use of the polar method, which accurately describes the bending behaviour of the studied plate wing with only six parameters. In the deterministic analysis of nominally orthotropic uncoupled laminated wings, the polar method allowed to even further reduce the dimension of the aeroelastic problem to only two bending polar parameters, thus giving a synthetic overview of the response surface of flutter critical velocity and highlighting the main physical phenomena. Particularly, the response surface exhibits a discontinuity which was found to be due to switching between aeroelastic modes as a consequence of the change in balance between longitudinal and torsional stiffness moduli. In addition, the optimum laminate for maximum flutter velocity is identified, which is situated exactly on the upper extremity of the discontinuity represented in the polar domain. In this case, the polar method is a useful tool to select significant layup configurations, located at different points of the polar domain, in order to analyse the influence of elastic symmetries, stacking sequences and mode switches on the stochastic aeroelastic response. The complexity of the present flutter response surface over the polar domain clearly demonstrates the need for uncertainty propagation in order to quantify

the effect of laminates' fabrication uncertainties in ply angles and thicknesses on the aeroelastic response of composite wings.

Moreover, the polar method allows to reduce the dimension of the stochastic problem from $2n_{\text{plies}}$ (*i.e.* twice the number of layers in the laminate, when considering randomness on angles and thicknesses) to the set $\boldsymbol{\theta}$ of only six modified bending polar parameters. It is thus possible to take into account the effect of elastic coupling arising from fabrication errors without any restriction on the uncertainty, such as forcing the resymmetrisation of the uncertain layup.

The uncertainty quantification was carried out using an arbitrary polynomial-chaos method that was adapted to handle the correlated random polar parameters. Moreover, it was augmented with a discontinuity detection based on machine learning in order to handle the mode switching. The method significantly reduced the number of calls to the aeroelastic solver by at least two orders of magnitudes compared to Monte Carlo simulations.

Even if small variabilities on ply angles and thicknesses are considered, coherently with the reduced tolerances of modern fabrication processes, the study showed that the nominal material properties of the layup are not preserved. Isotropic as well as anisotropic moduli are affected by uncertainties, elastic symmetries are lost, and the principal stiffness orientation $\Phi_1^{\tilde{D}}$ deviates from its nominal position, *i.e.* the span axis of the wing. This implies important deviations of the flutter velocity, which are especially large in the case of layups affected by the mode switch.

We were able to show that uncertainties in ply angles and thicknesses can give bi-modal distributions of the stochastic flutter velocity also in cases where their nominal layup is not situated directly on the modal discontinuity. The results of the uncertainty propagation highlight the need for robust aeroelastic optimisation of composite aeronautical structures, as the deviations from the nominal configurations easily exceed the classical 15% velocity margin if mode switches are encountered. Incorporating informations on uncertainties into the design process would thus provide additional safety, while potentially permitting performance gains in configurations that are situated in smooth regions.

Appendix A. Uncertainty quantification method

The basic technique of uncertainty quantification is Monte Carlo simulation. It is easy to implement, because it just requires propagating a number of realisations of the input parameters through the computational model. However, in order to obtain meaningful statistic results, a high number of samples is needed, which often renders its computational cost prohibitive. In order to alleviate the computational burden of Monte Carlo simulation, polynomial chaos approaches are employed, which we adopted in the present work. In order to reduce the dimension of the stochastic space to manageable numbers, the polar method is used. To handle the resulting non-trivial correlated distributions, we employ an adapted polynomial chaos approach by Navarro et al. [37].

Appendix A.1. Arbitrary Polynomial Chaos (aPC)

Polynomial chaos creates a response surface by using a spectral expansion in the stochastic space [56]

$$u(\boldsymbol{\theta}) = \sum_{i=1}^{M} \hat{u}_i \Phi_i(\boldsymbol{\theta}) \tag{A.1}$$

where Φ_i are orthogonal polynomials and $\hat{u}_i$ are the expansion coefficients by which these functions are weighted. The function of interest u corresponds in this case to the critical flutter velocity V_f, and the stochastic parameters $\boldsymbol{\theta}$ are the uncertain polar parameters.

The number of terms M depends on the number of parameters N, and the order of the polynomials [33]

$$M = \frac{(P+N)!}{P!N!} - 1 \tag{A.2}$$

This number of terms is rapidly increasing with the number of dimensions. The reduction of the number of dimensions obtained by the use of the polar method is consequently a key to render polynomial chaos applicable to problems in composite materials.

Originally, polynomial chaos was developed for Gaussian distributions, which uses Hermite polynomials [28] and then extended to different families of distributions summarised in the Askey scheme [29]. As the convergence of the method relies mostly on the orthogonality of the underlying polynomials, Soize and Ghanem [36] proposed an extension to arbitrary probability measures. However, this was rarely applied to correlated variables. To make the framework applicable to the correlated polar parameters which moreover has non-trivial distributions, this work will follow a recent example by Navarro, M.I. et al. [37], where the Gram-Schmidt algorithm is used to produce an orthogonal basis on correlated variables.

The orthogonality of the polynomials is defined in the sense of a scalar product which is noted as follows

$$\langle \phi_i, \phi_j \rangle = \int_{\boldsymbol{\Theta}} \phi_i(\boldsymbol{\theta}) \phi_j(\boldsymbol{\theta}) p(\boldsymbol{\theta}) d\boldsymbol{\theta} = \mathbb{E}\{\phi_i(\boldsymbol{\theta})^2\} \delta_{ij} \tag{A.3}$$

In order to orthogonalise the M polynomials with respect to this scalar product, the Gram-Schmidt algorithm calculates the coefficients of the polynomials using the scalar product itself, to ensure each polynomial is orthogonal to all of its predecessors [37]

$$\phi_0(\boldsymbol{\theta}) = 1 \tag{A.4}$$

$$\phi_j(\boldsymbol{\theta}) = e_j(\boldsymbol{\theta}) - \sum_{k=0}^{j-1} c_{jk} \phi_k(\boldsymbol{\theta}) \tag{A.5}$$

where $e_j = \{1, \theta_1, \theta_2, \dots, \theta_6, \theta_1^2, \theta_1\theta_2, \theta_1\theta_3, \dots\}$. The coefficients c_{jk} are computed as [37]

$$c_{jk} = \frac{\langle e_j(\boldsymbol{\theta}), \phi_k(\boldsymbol{\theta}) \rangle}{\langle \phi_k(\boldsymbol{\theta}), \phi_k(\boldsymbol{\theta}) \rangle} \tag{A.6}$$

where $\langle \cdot, \cdot \rangle$ denotes a polynomial scalar product as defined in Eq. (A.3). In [37] the coefficients are computed using moment-generating functions. To date, neither an analytical description of the joint distribution function nor characteristic or moment-generating function of the joint distribution of the polar parameters are available. Therefore, the necessary integrals are computed using Monte Carlo integration. Because this does not involve calls to the solver, but only evaluation of polynomials, this is computationally cheap.

The analytical description of the distribution functions not being available has another inconvenience. Normally in polynomial chaos expansions, the expansion coefficients are computed as [33]

$$\hat{u}_i = \frac{\langle u(\boldsymbol{\theta}), \phi_i(\boldsymbol{\theta}) \rangle}{\langle \phi_i(\boldsymbol{\theta}), \phi_i(\boldsymbol{\theta}) \rangle} \tag{A.7}$$

As the solver would need to be called for every sample, the Monte Carlo integration technique does not have any point in this case. Instead, the expansion coefficients are fitted using least-square regression on a random set of points in the parameter space [18].

A summary of the procedure used to calculate the response surface using the Gram-Schmidt type polynomial chaos is given in Fig. A.21.

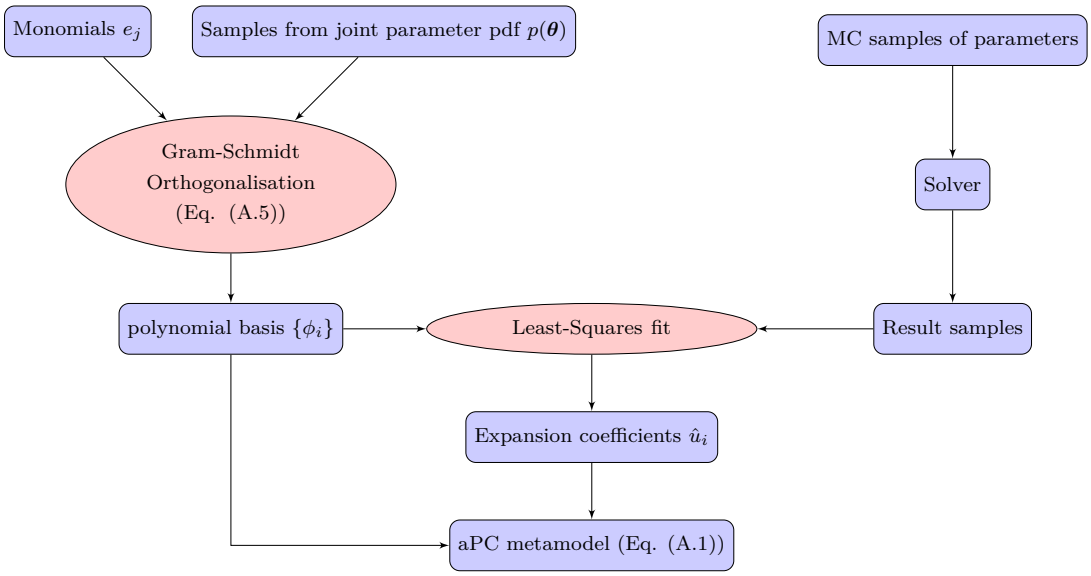

Figure A.21: Flowchart of the response surface construction using arbitrary polynomial chaos with Monte Carlo integration and least-square fitting of the expansion coefficients

Polynomials of order $P = 3$ were considered in the present work. The procedure has been validated in [55] against the test case of [37], where analytical solutions for an example problem are given. Moreover, for a certain choice of parameters, the input becomes uncorrelated, which enables further validation of the algorithm in comparison to classical Hermite polynomial chaos as investigated in [55].

Appendix A.2. Dealing with discontinuities in the response surface

Discontinuities in the flutter response with respect to material behaviour have been observed [18] which are due to changes in the modal regime. Global polynomial chaos does not perform well in that case [18]. In this work, we consider a simple solution to this problem consisting in separating regions of the response surface pertaining to different modal regimes and performing independent estimates of the response surface by polynomial chaos for each region. Instead of estimating the convex hulls of the modal regimes in the material parameter space [18], we use a machine learning-based filtering approach similar to [57] but applied to the arbitrary polynomial chaos approach described earlier. It has the advantage of being easier to automate and is able to cope with modal regimes of which the underlying material parameter space is non-convex, and also provides reasonable estimates for samples that fall outside of the domain covered by the preliminary sampling.

The combined procedure of machine learning and aPC basically consists of two steps. The first one is the identification of different modal regimes. In the second step, samples are filtered according to the information gained in the first step, which serves for the construction of the polynomials for the different regions of the response surface.

The first step is solved using the DBSCAN clustering algorithm [58], which clusters the samples by identifying high sample density zones in an environment which has low sampling density. It is applied on the preliminary samples of V_f and ω obtained by propagation through the aeroelastic solver, which are used later on for the fitting of the response surface. This procedure thus avoids additional calls to the aeroelastic solver. We employ the DBSCAN implementation

from *scikit-learn* as clustering algorithm [59], where we adjust the maximum core point distance and set the minimum cluster size to ten samples in order to avoid problems with outliers.

The clustering results, along with the associated polar parameters, are fed as training data into a classification algorithm. The classification algorithm serves afterwards as a filter to attribute subsequent samples of the polar parameters to the right region of modal regime. The filtered samples can then be used for the construction of the polynomials as well as sampling the reconstructed response surface. We performed the classification step by using the multi-layer perceptron neural-network classifier with its standard parameters, issued from that same *scikit-learn* library. A summary of how the algorithms are employed in the flutter problem is given in Fig. A.22.

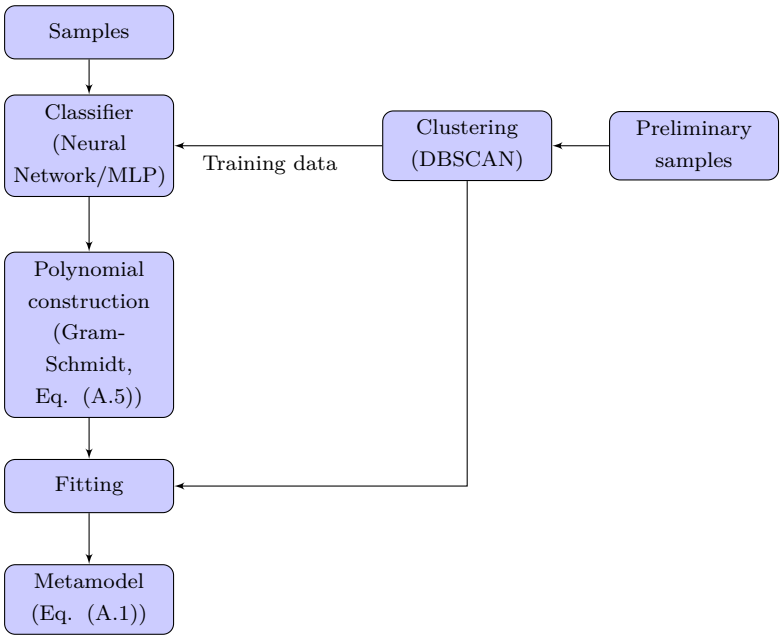

Figure A.22: Flowchart showing the use of machine learning for separation of the response surfaces

[1] J. Ashton, M. Waddoups, Analysis of Anisotropic Plates, Journal of Composite Materials 3 (1969) 148–165.

[2] Noor, A. K., Free vibrations of multilayered composite plates., AIAA Journal 11 (1973) 1038–1039.

[3] R. Ramkumar, T. Weisshaar, Flutter of flat rectangular anisotropic plates in high mach number supersonic flow, Journal of Sound and Vibration 50 (1977) 587–597.

[4] D. J. Mourey, Study of the feasibility aspects of flight testing an aeroelastically tailored forward swept research wing on a BQM-34F drone vehicle, Contractor Report CR-159149, National Aeronautics and Space Administration, 1979.

[5] T. A. Weisshaar, Aeroelastic Tailoring of Forward Swept Composite Wings, Journal of Aircraft 18 (1981) 669–676.

[6] T. A. Weisshaar, B. L. Foist, Vibration tailoring of advanced composite lifting surfaces, Journal of Aircraft 22 (1985) 141–147.

[7] D. Jensen, E. Crawley, J. Dugundji, Vibration of Cantilevered Graphite/Epoxy Plates With Bending-Torsion Coupling, Journal of Reinforced Plastics and Composites 1 (1982) 254–269.

[8] S. J. Hollowell, J. Dugundji, Aeroelastic flutter and divergence of stiffness coupled, graphite/epoxy cantilevered plates, Journal of Aircraft 21 (1984) 69–76.

[9] B. Landsberger, J. Dugundji, Aeroelastic behavior of straight and forward swept graphite/epoxy wings, in: 25th Structures, Structural Dynamics and Materials Conference, American Institute of Aeronautics and Astronautics, 1984.

[10] B. J. Landsberger, J. Dugundji, Experimental aeroelastic behavior of unswept and forward-swept cantilever graphite/epoxy wings, Journal of Aircraft 22 (1985) 679–686.

[11] G. I. Schueller, M. Shinozuka, L. Meirovitch, G. Oravas (Eds.), Stochastic Methods in Structural Dynamics, volume 10 of *Mechanics: Dynamical Systems*, Springer Netherlands, Dordrecht, 1987.

[12] S. Sriramula, M. K. Chryssanthopoulos, Quantification of uncertainty modelling in stochastic analysis of FRP composites, Composites Part A: Applied Science and Manufacturing 40 (2009) 1673–1684.

[13] C. Gogu, W. Yin, R. Haftka, P. Ifju, J. Molimard, R. Le Riche, A. Vautrin, Bayesian Identification of Elastic Constants in Multi-Directional Laminate from Moiré Interferometry Displacement Fields, Experimental Mechanics 53 (2013) 635–648.

[14] K. Sepahvand, M. Scheffler, S. Marburg, Uncertainty quantification in natural frequencies and radiated acoustic power of composite plates: Analytical and experimental investigation, Applied Acoustics 87 (2015) 23–29.

[15] K. Sepahvand, S. Marburg, Non-sampling inverse stochastic numerical and experimental identification of random elastic material parameters in composite plates, Mechanical Systems and Signal Processing 54-55 (2015) 172–181.

[16] C. L. Pettit, Uncertainty Quantification in Aeroelasticity: Recent Results and Research Challenges, Journal of Aircraft 41 (2004) 1217–1229.

[17] P. Beran, B. Stanford, C. Schrock, Uncertainty Quantification in Aeroelasticity, Annual Review of Fluid Mechanics 49 (2017) 361–386.

[18] C. Scarth, J. E. Cooper, P. M. Weaver, G. Silva, Uncertainty quantification of aeroelastic stability of composite plate wings using lamination parameters, Composite Structures 116 (2014) 84–93.

[19] S. W. Tsai, H. T. Hahn, Introduction to composite materials, Technomic Publ, Lancaster, Pa., 1980.

[20] G. Verchery, Les invariants des tenseurs d'ordre 4 du type de l'élasticité, in: Comportment Méchanique des Solides Anisotropes, volume 115, Editions du CNRS, Paris, Villard-de-Lans, 1979, pp. 93–104.

[21] P. Vannucci, Plane Anisotropy by the Polar Method, Meccanica 40 (2005) 437–454.

[22] A. Vincenti, M. R. Ahmadian, P. Vannucci, Optimization of laminated composites by using genetic algorithm and the polar description of plane anisotropy, Mechanics of Advanced Materials and Structures 20 (2013) 242–255.

[23] A. Jibawy, C. Julien, B. Desmorat, A. Vincenti, F. Léné, Hierarchical structural optimization of laminated plates using polar representation, International Journal of Solids and Structures 102 (2011) 55–78.

[24] C. Julien, Conception Optimale de l'Anisotropie dans les Structures Stratifiées à Rigidité Variable par la Méthode Polaire-Génétique, Ph.D. thesis, Sorbonne Universités, Université Pierre et Marie Curie Paris 6/CNRS, UMR 7190, Paris, 2010.

[25] P. Vannucci, A Note on the Elastic and Geometric Bounds for Composite Laminates, Journal of Elasticity 112 (2013) 199–215.

[26] M. Montemurro, A. Vincenti, P. Vannucci, A Two-Level Procedure for the Global Optimum Design of Composite Modular Structures—Application to the Design of an Aircraft Wing. Part 1: Theoretical Fomrulation, Journal of Optimization Theory and Applications 155 (2012) 24–53. URL: http://link.springer.com/10.1007/s10957-012-0070-1.

[27] M. Montemurro, A. Vincenti, P. Vannucci, A Two-Level Procedure for the Global Optimum Design of Composite Modular Structures — Application to the Design of an Aircraft Wing: Part 2: Numerical Aspects and Examples, Journal of Optimization Theory and Applications 155 (2012) 24–53. URL: http://link.springer.com/10.1007/s10957-012-0070-1.

[28] N. Wiener, The Homogeneous Chaos, American Journal of Mathematics 60 (1938) pp. 897–936. URL: http://www.jstor.org/stable/2371268.

[29] D. Xiu, G. E. Karniadakis, The Wiener–Askey Polynomial Chaos for Stochastic Differential Equations, SIAM Journal on Scientific Computing 24 (2002) 619–644.

[30] D. Xiu, G. E. Karniadakis, Modeling uncertainty in steady state diffusion problems via generalized polynomial chaos, Computer Methods in Applied Mechanics and Engineering 191 (2002) 4927–4948.

[31] D. Lucor, D. Xiu, C.-H. Su, G. E. Karniadakis, Predictability and uncertainty in cfd, International Journal for Numerical Methods in Fluids 43 (2003) 483–505.

[32] D. Xiu, D. Lucor, C.-H. Su, G. E. Karniadakis, Stochastic Modeling of Flow-Structure Interactions Using Generalized Polynomial Chaos, Journal of Fluids Engineering 124 (2002) 51.

[33] J. Le Meitour, D. Lucor, J.-C. Chassaing, Prediction of stochastic limit cycle oscillations using an adaptive Polynomial Chaos method, Journal of Aeroelasticity and Structural Dynamics 2 (2010) 1–20.

[34] M. Thapa, S. B. Mulani, R. W. Walters, A new non-intrusive polynomial chaos using higher order sensitivities, Computer Methods in Applied Mechanics and Engineering 328 (2018) 594–611.

[35] L. Mathelin, M. Y. Hussaini, T. A. Zang, Stochastic approaches to uncertainty quantification in CFD simulations, Numerical Algorithms 38 (2005) 209–236.

[36] C. Soize, R. Ghanem, Physical Systems with Random Uncertainties: Chaos Representations with Arbitrary Probability Measure, SIAM Journal on Scientific Computing 26 (2004) 395–410.

[37] Navarro, M.I., Witteveen, J.A.S., Blom, J.G., Polynomial Chaos Expansion for general multivariate distributions with correlated variables, Technical Report, Centrum Wiskunde & Informatica, 2014. URL: https://repository.cwi.nl/noauth/search/fullrecord.php?publnr=22484.

[38] S. Dey, T. Mukhopadhyay, H. H. Khodaparast, S. Adhikari, Fuzzy uncertainty propagation in composites using Gram–Schmidt polynomial chaos expansion, Applied Mathematical Modelling 40 (2016) 4412–4428.

[39] K. Sepahvand, Spectral stochastic finite element vibration analysis of fiber-reinforced composites with random fiber orientation, Composite Structures 145 (2016) 119 – 128. URL: http://www.sciencedirect.com/science/article/pii/S0263822316301106. doi:https://doi.org/10.1016/j.compstruct.2016.02.069.

[40] O. Stodieck, J. E. Cooper, P. M. Weaver, P. Kealy, Improved aeroelastic tailoring using tow-steered composites, Composite Structures 106 (2013) 703–715. URL: http://linkinghub.elsevier.com/retrieve/pii/S0263822313003462.

[41] W. Stein, A summary of Classical Lamination Theory, 2010. URL: http://wstein.org/edu/2010/480b/projects/05-lamination_theory/A%20summary%20of%20Classical%20Lamination%20Theory.pdf, retrieved on February 25th, 2015.

[42] M. D. Minich, C. C. Chamis, Analytical displacements and vibrations of cantilevered unsymmetric fiber composite laminates, in: AIAA, ASME, and SAE, Structures, Structural Dynamics, and Materials Conference, Denver, Colorado, 1975.

[43] A. W. Leissa, The free vibration of rectangular plates, Journal of Sound and Vibration 31 (1973) 257–293.

[44] J. R. Wright, J. E. Cooper, Introduction to aircraft aeroelasticity and loads, 2. ed ed., Wiley, Chichester, 2015.

[45] J. N. Reddy, Theory and analysis of elastic plates, Taylor & Francis, Philadelphia, PA, 1999.

[46] Z. Gurdal, R. Haftka, P. Hajela, Design and optimization of laminated composite materials, Wiley, New York, 1999.

[47] H. Ghiasi, D. Pasini, L. Lessard, Optimum stacking sequence design of composite materials part i: constant stiffness design, Composite Structures 90 (2009) 1–11.

[48] H. Ghiasi, D. Pasini, L. Lessard, Optimum stacking sequence design of composite materials part ii: variable stiffness design, Composite Structures 93 (2010) 1–13.

[49] P. Vannucci, A Special Planar Orthotropic Material, Journal of elasticity and the physical science of solids 67 (2002) 81–96.

[50] U.S. Department of Defense, COMPOSITE MATERIALS HANDBOOK, U.S. Department of Defense, 2002.

[51] S. J. Hollowell, Aeroelastic flutter and divergence of graphite/epoxy cantilevered plates with bending-torsion stiffness coupling, Master's thesis, Massachusetts Institute of Technology, Dept. of Aeronautics and Astronautics, 1981.

[52] J. A. Witteveen, S. Sarkar, H. Bijl, Modeling physical uncertainties in dynamic stall induced fluid–structure interaction of turbine blades using arbitrary polynomial chaos, Computers and Structures 85 (2007) 866 – 878. URL: http://www.sciencedirect.com/science/article/pii/S0045794907000168. doi:https://doi.org/10.1016/j.compstruc.2007.01.004, fourth MIT Conference on Computational Fluid and Solid Mechanics.

[53] S. Oladyshkin, W. Nowak, Data-driven uncertainty quantification using the arbitrary polynomial chaos expansion, Reliability Engineering and System Safety 106 (2012) 179 – 190. URL: http://www.sciencedirect.com/science/article/pii/S0951832012000853. doi:https://doi.org/10.1016/j.ress.2012.05.002.

[54] J. A. Paulson, E. A. Buehler, A. Mesbah, Arbitrary polynomial chaos for uncertainty propagation of correlated random variables in dynamic systems, IFAC-PapersOnLine 50 (2017) 3548 – 3553. URL: http://www.sciencedirect.com/science/article/pii/S240589631731426X. doi:https://doi.org/10.1016/j.ifacol.2017.08.954, 20th IFAC World Congress.

[55] C. T. Nitschke, Quantification of aleatory and epistemic uncertainties in the prediction of aeroelastic instabilities, Ph.D. thesis, Sorbonne Universités, Institut Jean Le Rond d'Alembert, CNRS UMR 7190, Paris, 2018.

[56] D. Lucor, Introduction to Uncertainty Quantification in Computational Fluid Dynamics, 2012. Lecture Notes of NSE22 2012, held at Université Pierre et Marie Curie Paris 6.

[57] C. Scarth, P. N. Sartor, J. E. Cooper, P. M. Weaver, G. H. C. Silva, Robust and Reliability-Based Aeroelastic Design of Composite Plate Wings, AIAA Journal 55 (2017) 3539–3552.

[58] M. Ester, H.-P. Kriegel, J. Sander, X. Xu, A density-based algorithm for discovering clusters in large spatial databases with noise., in: Proceedings of the Second International Conference on Knowledge Discovery and Data Mining, volume 96, 1996, pp. 226–231.

[59] F. Pedregosa, G. Varoquaux, A. Gramfort, V. Michel, B. Thirion, O. Grisel, M. Blondel, P. Prettenhofer, R. Weiss, V. Dubourg, J. Vanderplas, A. Passos, D. Cournapeau, M. Brucher, M. Perrot, E. Duchesnay, Scikit-learn: Machine Learning in Python, Journal of Machine Learning Research 12 (2011) 2825–2830.